6-2013

# Proton Induced X-ray Emission Spectrometry of Atmospheric Aerosols at Piseco Lake

Adam Margulies
*Union College - Schenectady, NY*

Proton Induced X-ray Emission Spectrometry of Atmospheric Aerosols at
Piseco Lake


By

Adam Zeldes Margulies



\*\*\*\*\*\*\*\*\*\*\*



Submitted in Partial Fulfillment
of the Requirements for
Honors in the Department of Physics and Astronomy



UNION COLLEGE
June, 2013

# Table of Contents

**Abstract:** Chemical studies of lakes and aerosols in the Adirondack region of New York State have found evidence of environmental pollution resulting in acid rain. We obtained air samples for July and September 2012 from Piseco Lake and analyzed particulate depositions with Proton Induced X-ray Emission (PIXE) spectrometry. We detected an array of light elements, including sulfur particulates in the 0.25 - 8 μm range, possibly stemming from coal combustion in the Appalachians and Mid-West of the United States. We also found systematic errors with the accelerator charge integration system due to beam spreading after the beam passes through the target. This alerted us to the need for a Faraday cup with greater cross-sectional area to collect all of the charge that passes through the target.

## Introduction and Theory

It is well documented that air pollution adversely affects ecosystems within the Adirondack region of New York [1 - 2]. Numerous chemical studies have been performed in an effort to quantify the environmental damage [3]. In addition to academic and privately funded research, the New York State Department of Environmental Conservation (DEC) uses a network of 20 monitoring sites to measure acid deposition [4]. We set out to analyze the elemental composition of particulate matter (PM) in aerosols at the Piseco Lake site with Proton-Induced X-ray Emission (PIXE) spectrometry. We hope that this study will supplement existing chemical analyses and motivate future research in this field.

PIXE spectrometry is a technique used for determining elemental concentrations in a material, and is particularly well suited for environmental studies. Discovered in 1913 by Moseley and popularized in the 1970s by Johansson, Campbell and Malmqvist, the technique proceeds by bombarding a target with a moderately energetic ($\sim$ MeV) proton beam [5 - 6]. As a proton comes into close proximity with an atom inside the material, there is a probability, determined by the ionization cross-section, that the atom will lose an electron. In this instance, an electron from a higher energy state will de-excite to fill the vacancy, which may be in the K-shell (ground state, or n = 1), L-shell (first excited state, or n = 2), or higher. As seen

below in Figure 1, each transition to a specific shell has further discrete energy levels, denoted α, β, γ, etc., which in turn have more sub-levels, depending on the initial state of the electron filling the vacancy.  Within each shell, the α-transition is the least energetic, and therefore the most probable.
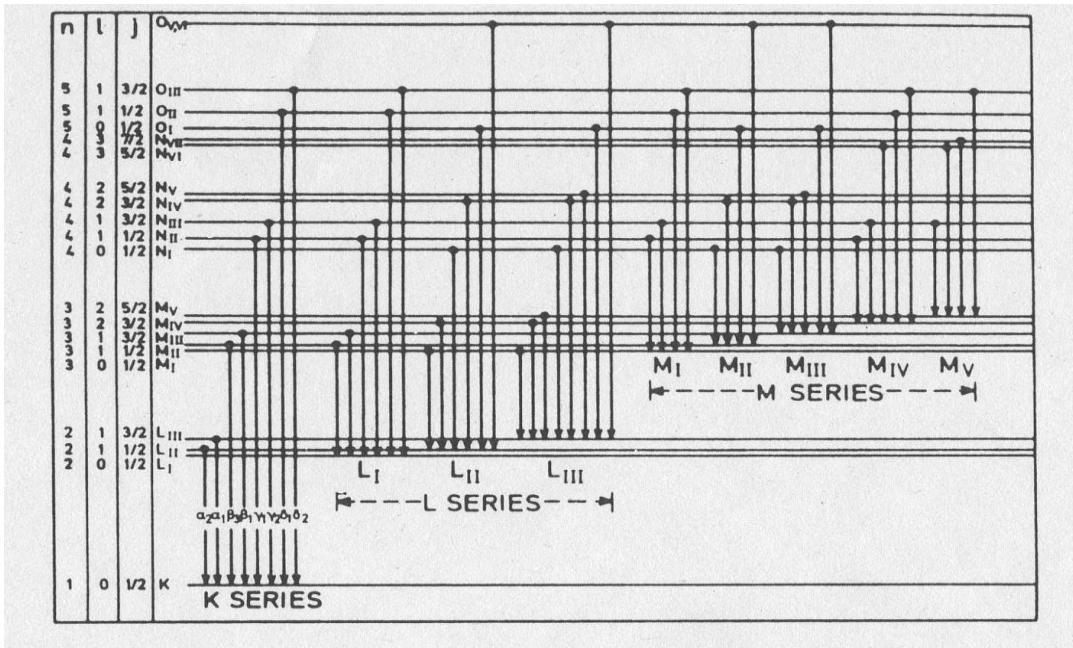


**Figure 1**. Generic model of K, L, and M series electron transitions.  Quantum mechanical properties are designated by values of n, l, and j (left) [7].

The resultant X-ray is emitted with an energy given by the relation,

$$E_{x-ray} = E_{\text{initial state}} - E_{\text{final state}}$$

Eq. 1

Additionally, we may derive an approximate X-ray energy using the Bohr Model, where an electron's energy may be considered as the sum of its kinetic and potential energies.  Moseley empirically found that the electron's energy was proportional to $(Z - 1)^2$, where Z is the atomic

number of the element.[1]  Treating the kinetic and potential energies in the context of the

Coulomb interaction between the electron and the nucleus, we get,

$$E = K + V \qquad\qquad \text{Eq. 2}$$

$$= \frac{m(Z-1)^2 e^4}{2(4\pi\varepsilon_o)^2 n^2 \hbar^2} - \left[ -\frac{m(Z-1)^2 e^4}{(4\pi\varepsilon_o)^2 n^2 \hbar^2} \right] \qquad\qquad \text{Eq. 3}$$

$$= -\left( \frac{m e^4}{2(4\pi\varepsilon_o)^2 \hbar^2} \right) \frac{(Z-1)^2}{n^2}, \qquad\qquad \text{Eq. 4}$$

where $m$ = 510.999 eV/c$^2$ is the mass of the electron, $e$ = 1.602 $x$ 10$^{-19}$ C is the charge of the

electron, $\varepsilon_o$ = 8.854 $x$ 10$^{-12}$ C$^2$·N$^{-1}$·m$^{-2}$ is the permittivity of free space, $n$ is the principle quantum

number of the electron, and $\hbar$ = 6.58 $x$ 10$^{-16}$ eV·s is Planck's constant over 2π.  We observe that

Eq. 4 is negative, which signifies that the electron is in a bound state within the atom.  We may

now combine Eq. 4 and Eq. 1 to obtain,

$$E_{\text{x-ray}} = E_{\text{initial state}} - E_{\text{final state}} = -13.57 eV (Z-1)^2 \left[ \frac{1}{n_{\text{final}}^2} - \frac{1}{n_{\text{initial}}^2} \right]. \qquad \text{Eq. 5}$$

Moseley used Eq. 5 to plot Z as a function of the square root of X-ray frequency (and hence the

square root of energy).  Seen in Figure 2, he used this method to determine the range of

elements that are likely to radiate in a given X-ray series (K, L, etc.).

---

[1] Moseley attributed this relationship to the effects of screening, an explanation that was later refuted in favor of quantum mechanical considerations [8 - 9].
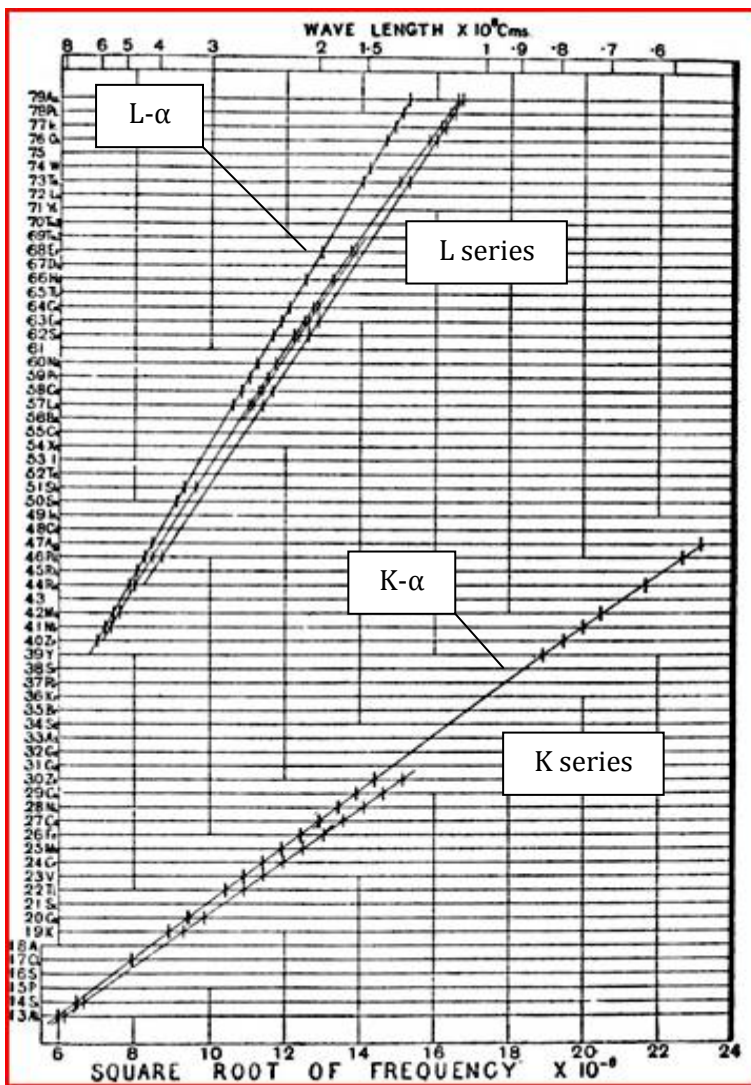
**Figure 2**. Moseley's original plot of characteristic X-rays. The lower linear fits represent K-series emissions while the upper fits represent L-series emissions. The α-line is highest for each set of fits [5].

As seen in Figure 2, we are unlikely to detect L-series X-rays in our study unless elements heavier than Yitrium (Z = 39) exist in the aerosols. We used the ranges displayed in Figure 2 and compared our data to a table of K and L series X-ray energies to determine Z, and therefore the elemental composition of the sample.

## Methods and Materials

We used a PIXE International nine-stage cascade impactor, shown below in Figure 3, to collect aerosol deposits categorically by size [10]. 6.3µm thick kapton foils collected particles at the first nine stages, and an 11µm thick nuclepore filter collected particles that reached the bottom of the impactor. In order to reduce static charge collected on the kapton foils and the nuclepore that could affect a measurement of the mass, we irradiated each with five minute exposures to [241]Am, an α-emitter, at a distance of approximately 1 cm. We measured the masses of the foils and the nuclepore before and after sample collection.[2]
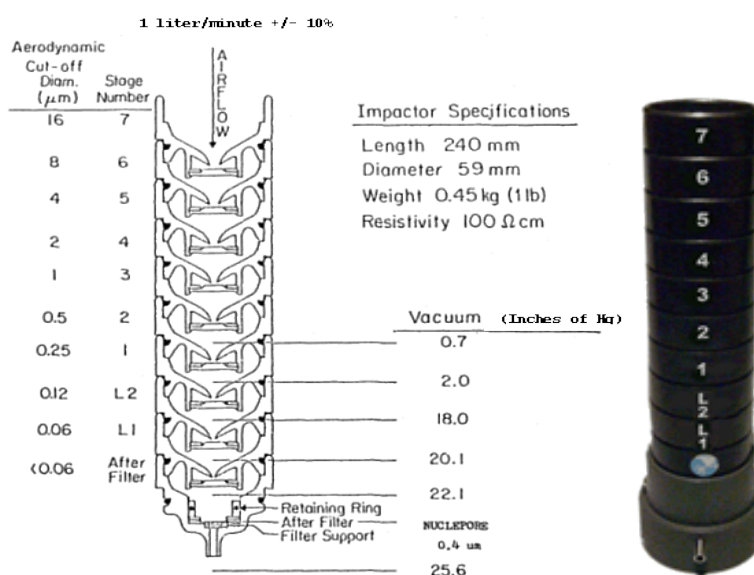


**Figure 3**. A diagram (left) and photograph (right) of the PIXE International nine-stage cascade impactor [10].

After cleaning and preparing the impactor, we installed the kapton foils and positioned it near Piseco Lake, away from articifical contaminants. This set-up is seen below in Figure 4.

---

[2] As our measurements after collection did not support the conclusion that any matter was collected, we were unable to use this part of the experimental procedure later in our analysis. We will attempt this again in the future to complete a gravinometric analysis.

The impactor was attached to a vacuum pump, which drew in air at a rate of 1L/min for approximately 48 hours. In total, the impactor processed 2.88 m$^3$ of air.



**Figure 4**. The impactor, encased in a white protective shell, is mounted in the woods at the Piseco Lake site.

Prior to collecting PIXE spectra from the aerosol samples, we needed to 1) calibrate the detection system energy spectra acquired by the MCA software; and 2) obtain PIXE spectra from standards to determine *H*, an experimental constant equal to the solid angle of the detector (see p. 11-13 below) [11]. To achieve our first objective, we placed a radioactive [214]Am source on the Union College silicon drift detector (SDD) [12-13]. The energy spectrum and relevant peak information are shown below in Figure 5 and Table 1, respectively.
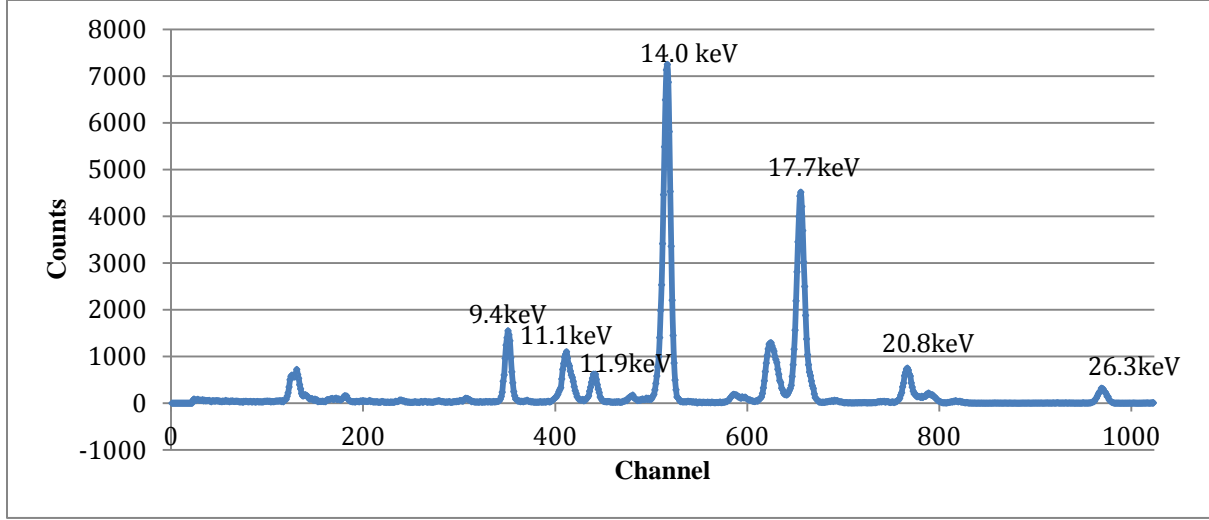
**Figure 5**. An X-ray energy spectrum obtained from the [241]Am calibration source.

| Centroid Channel Position c(E) | E (keV) | FWHM (channels) | $\sigma(E)^2 = \frac{FWHM^2}{8ln(2)}$ |
|---|---|---|---|
| 350 | 9.441 | 4.0 | 2.885 |
| 411 | 11.069 | 5.5 | 5.455 |
| 440 | 11.887 | 4.5 | 3.652 |
| 515 | 13.992 | 4.5 | 3.652 |
| 655 | 17.747 | 5.0 | 4.508 |
| 766 | 20.781 | 5.0 | 4.508 |
| 969 | 26.345 | 6.0 | 6.492 |

**Table 1**. Centroid channel numbers, known energies, full-width-half maxima (FWHM), and standard deviations squared ($\sigma^2$) for the calibration peaks.

Each X-ray energy $E$ corresponds to a centroid channel position $c(E)$ via the following

relation,

$$c(E) = A_1 + A_2E + A_3E^2,$$
<div align="right">Eq. 6</div>

where $A_1$ and $A_2$ are the fit parameters of interest and we set $A_3 = 0$ [11]. Neglecting the $A_3$

term is allowed since the electronics processed the energy per channel linearly, as seen below

in Figure 6, where we have plotted $c(E)$ vs. $E$. In cases where the fit is non-linear, this may be

corrected with a small $A_3$ term. From the regression, we determined $A_1 = 36.618$, $A_2 = 4.539$.
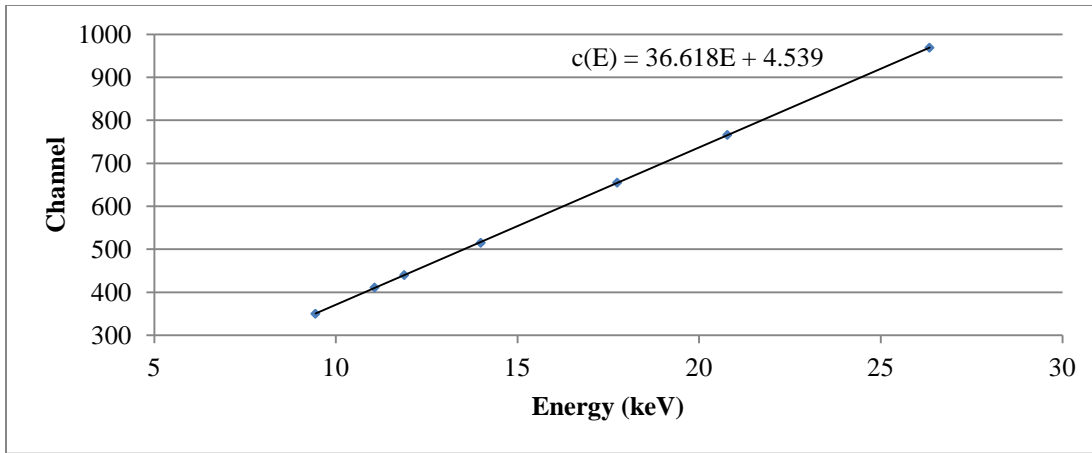
**Figure 6**. A plot of X-ray energy (E) vs. channel number (c) for the [241]Am calibration source.

The two remaining parameters, $A_4$ and $A_5$, were used by our analysis software (see p. 11 below) to position every peak in the energy spectrum and characterize their widths. We determined them by utilizing the following relation,

$$\sigma(E)^2 = A_4 + A_5 E, \qquad\qquad \text{Eq. 7}$$

and plotting $\sigma(E)^2$ vs. $E$, as seen below in Figure 7[3] [11]. We computed $A_4 = 1.067$, $A_5 = 0.193$.
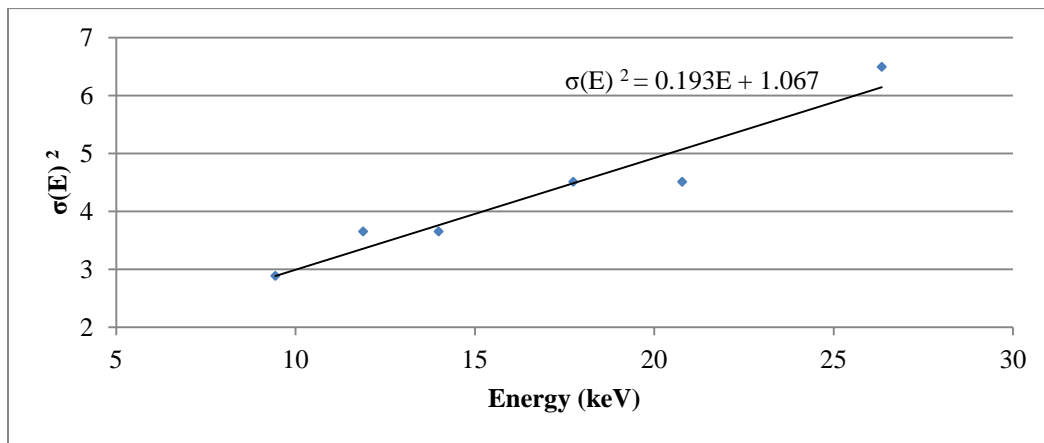


**Figure 7**. A plot of X-ray energy (E) vs. standard deviation squared ($\sigma^2$) for the [241]Am calibration source.

---

[3] Here we discarded data from the peak at channel 411, as the width of this peak was anomalous in our data set.

After we determined our fit parameters, we obtained PIXE spectra for four single-element standards, Titanium, Iron, Copper, and Germanium, by accelerating a 2.2 MeV proton beam at each standard with the Union College Pelletron Particle Accelerator.  To generate the beam, hydrogen gas was first bled into a quartz bottle, where it was ionized by a 100 MHz radio frequency discharge as seen in the schematic shown in Figure 8.  A 2200 V bias accelerated the proton beam out of the bottle toward the ion source.  We used an electric field to do work on the beam, thereby injecting it into a rubidium charge exchange cell.  As each proton moved through the heated vapor, it gained two electrons through charge exchange collisions with the rubidium.  The negative ion beam then entered the accelerator.
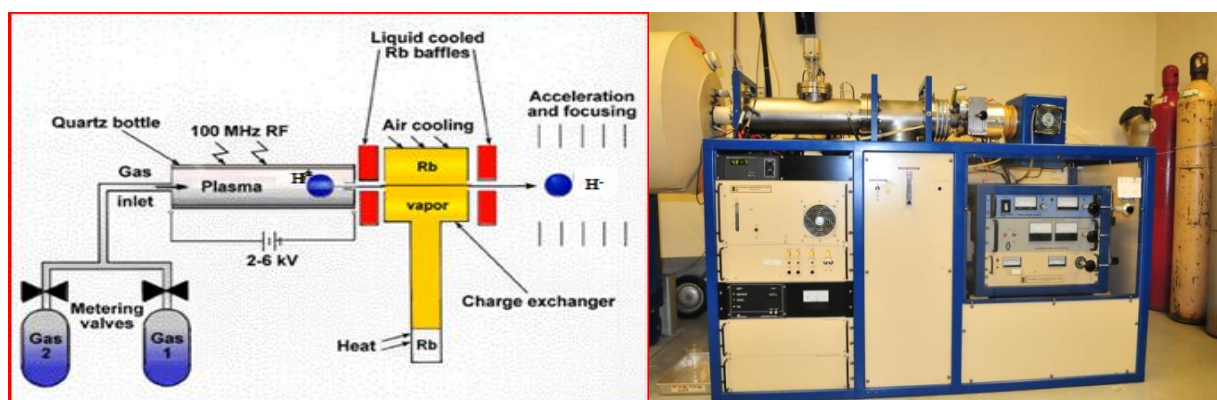


**Figure 8**. Ion source for the Union College Pelletron Accelerator.  Left: schematic of the ion source and charge exchanger for the positive to negative ion configuration; right: photo of ion source [12 - 13].

Once at the tank center (the Pelletron terminal), the negative ions were accelerated through a 1.1 MV potential.  The accelerator itself is a tandem electrostatic machine, and the charge in the terminal was generated via induction with a chain consisting of alternating metal pellets and insulating links.   In Figure 9, the Pelletron charging system is shown in schematic next to a photograph of the accelerator column with the tank shell removed.  The negatively charged inductor electrode stripped electrons from the pellets while they were touching the

grounded drive pulley.  As the chain transferred the pellets from the low-energy end of the

terminal to the high-energy end, the net positive charge was retained due to the presence of

the induction field.  At the high-energy end of the terminal, the process was reversed.  When

the chain reached the terminal, it passed through a negatively biased suppressor electrode that

ensured no arcing occurred as the pellets came into contact with the terminal pulley.  Thus, as

the pellets exited the suppressor, charge flowed smoothly onto the terminal pulley, making the

terminal positively charged.  Concurrent to these processes, a bottle located at the high-energy

end of the column bled nitrogen gas into the terminal.  As the negatively charged ion beam

passed through the terminal, electrons were stripped away in charge exchange collisions with

the nitrogen gas.  This allowed the now positive beam to accelerate away from the positively

charged terminal shell.   The total work done on the completely stripped ions in the accelerator
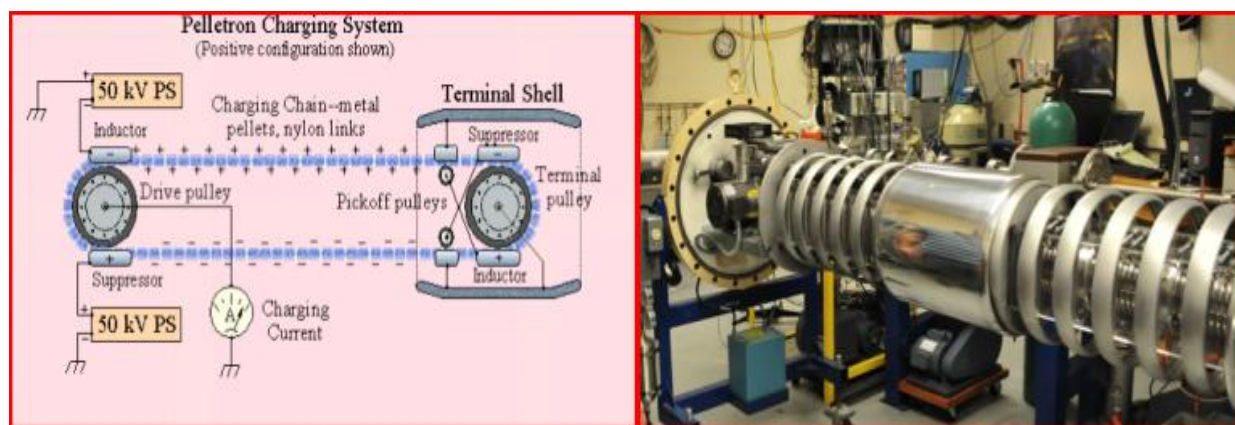
was approximately 2.2 MeV.



**Figure 9**. Union College Pelletron Terminal.  Left: schematic of the charging system, showing
the chain and motor assembly [14].  Right: photograph of the accelerator column with the tank
shell removed [13].  The ion beam enters from right side of the column (low-energy end) and
exits on the left (high-energy end).

After the proton beam left the accelerator, it was magnetically steered into the

scattering chamber, which housed a 3-slot ladder containing the target material (e.g., for the

first runs, three of the four standards).  The scattering chamber and ladder are shown in Figure

10.  We refocused the beam on a different slot in the ladder for each run by using target

manipulator,  display screen and predetermined coordinates for the centers of the targets.  For

each standard and aerosol sample, we collected 1μC of total charge, counted by a charge

integrator after the charge collected in the Faraday cup passed the target at the end of the
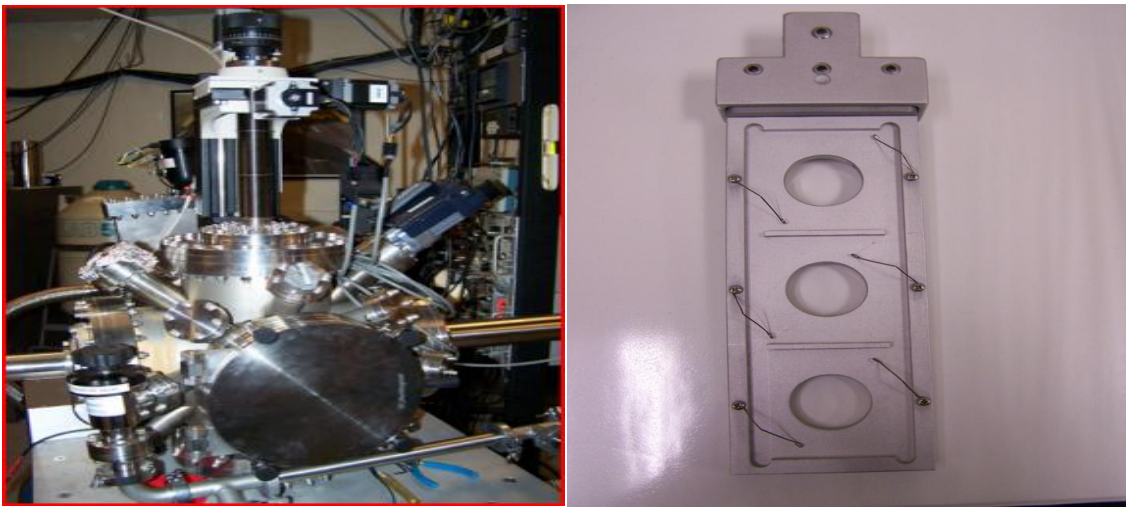
beam line.



**Figure 10**.  Left: Union College Pelletron endstation.  The target manipulator can be seen
above the scattering chamber.  Right: 3-slot target ladder (empty) [15].

We used a PIXE analysis software package, GUPIX, to analyze the X-ray spectra [16].

When we ran the program for a given standard or aerosol sample, GUPIX calculated the

concentrations $C_z$ in ng/cm$^2$ of an element (for $11 \leq Z \leq 92$) using the following formula:

$$C_z = \frac{Y_Z}{(Y_T)(H)(Q)(\varepsilon)(T)},$$

Eq. 8

where $Y_Z$ is the intensity of the principle X-ray line for element Z, $Y_T$ is the theoretical intensity,

$H$ is the experimental constant defined above, $Q$ is the total charge collected, ε is the efficiency

of the detector, and $T$ is the transmission coefficient through any filters or absorbers between

the sample and the X-ray detector [11]. When running on the standards, we originally set H = 1. Since the remaining terms on the right side of Eq. 8 remained constant, we were able to calculate the correct value of H for any element using the ratio of the known elemental concentration in a standard, $C_{Z\ known}$, to the unadjusted concentration, $C_{z\ H=1}$, calculated by GUPIX (Eq. 9).

$$H = \frac{C_{Z\ H=1}}{C_{Z\ known}} \qquad\qquad \text{Eq. 9}$$

Since the detector was not moved, the X-ray spectra for the standards should not have change over time; but we obtained spectra prior to both the July and September air samplings as a check. Table 2 shows the September H values determined from Eq. 9, the unadjusted GUPIX elemental concentrations $C_{z\ H=1}$ from Eq. 8, and the known concentrations for each standard.

| Standard | $C_{Z\ known}$ (ng/cm$^2$) | $C_{Z\ H=1}$ (ng/cm$^2$) | $H$ |
|---|---|---|---|
| Ti | 5.69E+04 | 104.3 | 1.83E-03 |
| Fe | 5.48E+04 | 134.1 | 2.45E-03 |
| Cu | 6.05E+04 | 130.1 | 2.15E-03 |
| Ge | 4.93E+04 | 101.2 | 2.05E-03 |

**Table 2**. September 2012: Known concentrations, H = 1 concentrations, and H values for Ti, Fe, Cu, Ge.

We plotted $H$ vs. $Z$ (Figure 11) for both months and confirmed that the $H$ values were roughly constant, and not linearly dependent on $Z$. H values that remain constant over the Z range are desirable, as H represents the solid angle of the detector, which does not change as a function of Z.[4] As seen below, we did not use Germanium as a standard in July. Data from both

---

[4] According to the GUPIX manual, small Z-dependencies in H may arise due to database imperfections or imperfect knowledge of filters or absorbers or detector efficiency [11]. GUPIX therefore allows the user to input appropriate H versus X-ray energy values in the program when H is not constant. Since we found H to be roughly constant, we did not use this method.

months exhibit the same non-linear behavior; however, there is a clear shift in the values, which will be discussed later in our error analysis. We averaged over both months to get a final value, $H = 2.483 \times 10^{-3}$, that we used in our analysis of both the July and September aerosols.
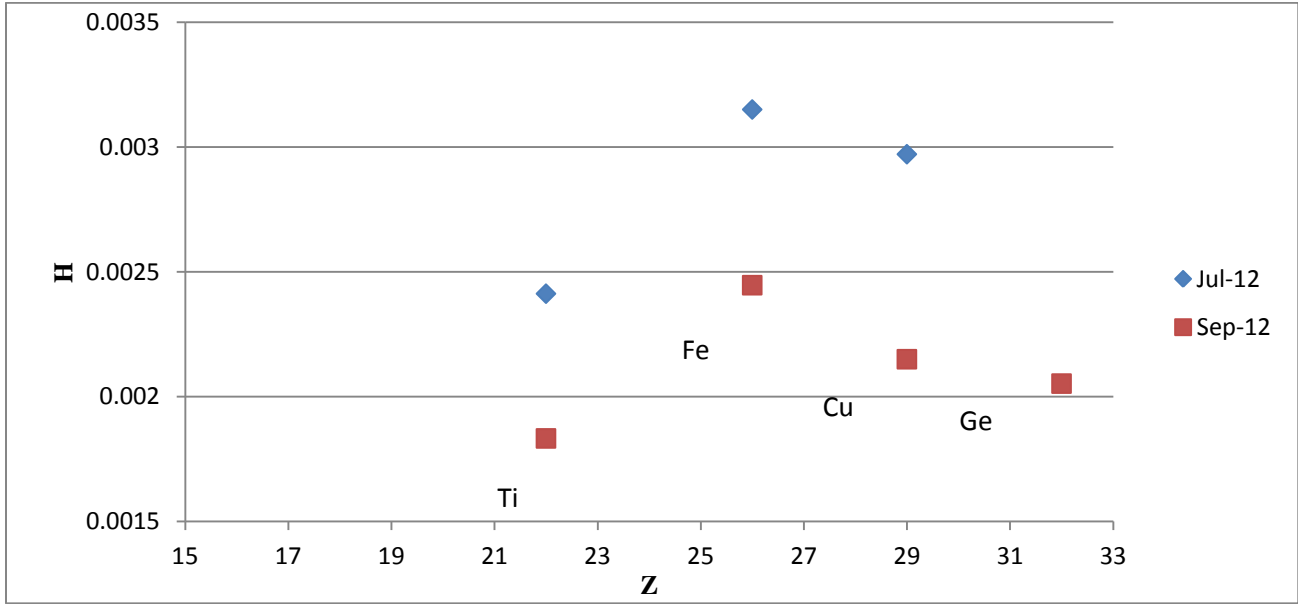


**Figure 11**. Constant $H$ *vs* $Z$ relationship for standards prior to July and September air samples.

After running GUPIX on the aerosol samples, we converted the areal mass density concentrations calculated by GUPIX to mass per unit volume concentrations $C_v$. This relation is given by

$$C_v = \left(\frac{P_{\text{SATP}}\, T}{T_{\text{SATP}}\, P}\right) \frac{A}{f \Delta t} C_A, \qquad \text{Eq. 10}$$

where $T_{\text{SATP}} = 298$ K and $P_{\text{SATP}} = 760$ mm Hg are the standard ambient temperature and pressure, respectively; $T$ and $P$ are the average temperature and pressure, respectively, at the sampling site while the impactor pump is running; $A$ is the area of the particulate deposit on the impaction foil, $f = (1.0 \pm 0.1)$ L/min is the flow rate of the pump, and $\Delta t = (48 \pm 1)$ hours is

the amount of time that the pump was running.  We calculated $T$ and $P$ by averaging over data recorded at approximately hour intervals throughout the 48 hours, and we estimated uncertainties for $T$ and $P$ according to the variations in pressure and temperature.[5]  For July, we found $T$ = (299 ± 5) K, $P$ = (760.0 ± 0.9) mm Hg; and for September, we found $T$ = (293 ± 3) K, $P$ = (757.3 ± 0.9) mm Hg.  Approximating the shape of the deposits as circles, we used an Olympus SZ61 optical microscope and Stream Basic Olympus Soft Imaging Solutions software to find the areas.  Particulate samples for stages 1 – 5 are shown under the microscope below in Figure 12, with accompanying areas in Table 3.  The values in Table 3 are the average of four measurements, two for the smallest inclusive circle, and two for the largest inclusive circle. We obtained our uncertainties by finding the difference between the mean area and the maximum area, the difference between the mean area and the minimum area, and averaging.
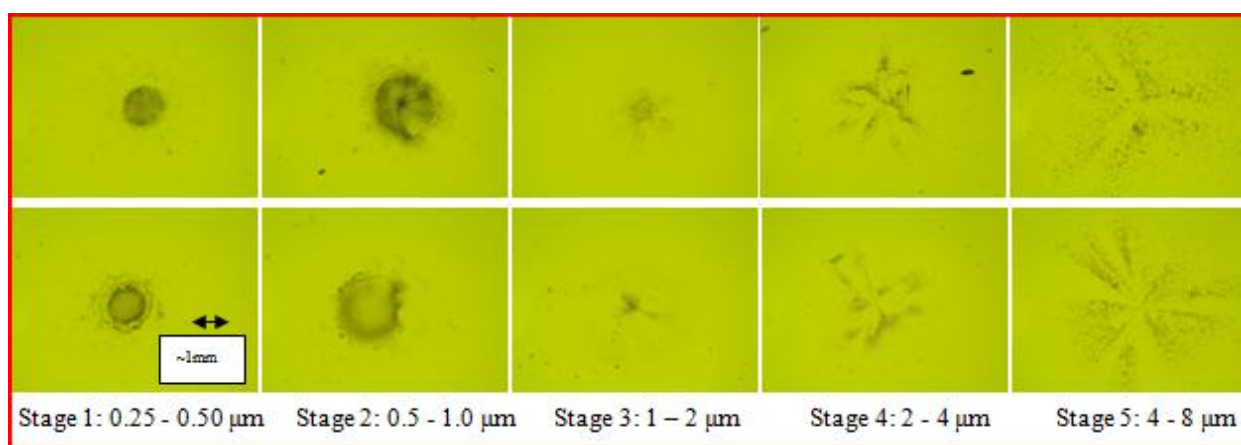


**Figure 12**. Particulate deposits on kapton foils for July (top) and September (bottom) aerosols.

---

[5] The database we used to find hourly temperatures and pressures can no longer be accessed.  For a database from a similar weather service that archives all records from nearby Rome, NY, see [17].

| $A \pm \Delta A$ (μm$^2$) x 10$^6$ | | | | | |
|---|---|---|---|---|---|
| Particle size range | Stage 1: 0.25-0.50μm | Stage 2: 0.5 -1.0μm | Stage 3: 1-2μm | Stage 4: 2-4μm | Stage 5: 4-8μm |
| July 2012 | 2.5 ± 0.7 | 5 ± 2 | 5 ± 2 | 20 ± 5 | 33 ± 8 |
| September 2012 | 4 ± 2 | 8 ± 2 | 3 ± 2 | 15 ± 2 | 29 ± 6 |

**Table 3**. Areas of particulate deposits on kapton foils for July and September aerosols.

Kapton foils in stages 6 (8 – 16 μm), 7 (>16 μm), L2 (0.12 – 0.25 μm), L1 (0.06 – 0.12 μm), and the nuclepore (<0.06 μm) did not accumulate a sufficient number of particles for us to discern a significant deposit under the microscope.[6]

## IV. Results

For each impaction foil, we plotted X-ray energy vs. counts in linear and log scales. All plots are shown in Appendix 1. By way of example, both stage 1 spectra for September are shown below in Figures 13 and 14, with clear K-shell X-ray peaks labeled. We are most interested in peaks from aerosol samples (blue) that are above the kapton background (red).

---

[6] The lack of physical evidence for these stages mainly agreed with the concentrations found by GUPIX.
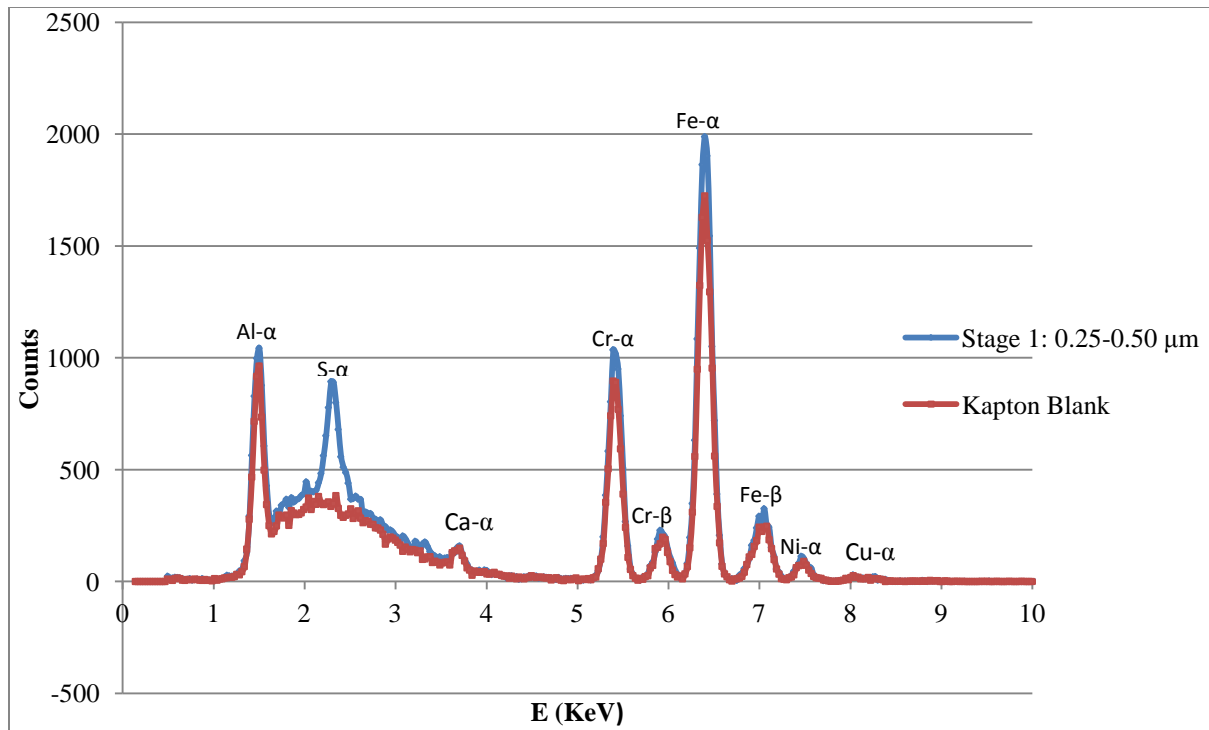
**Figure 13**. September 2012 stage 1 (PM 0.25-0.50): X-ray energy vs. counts.
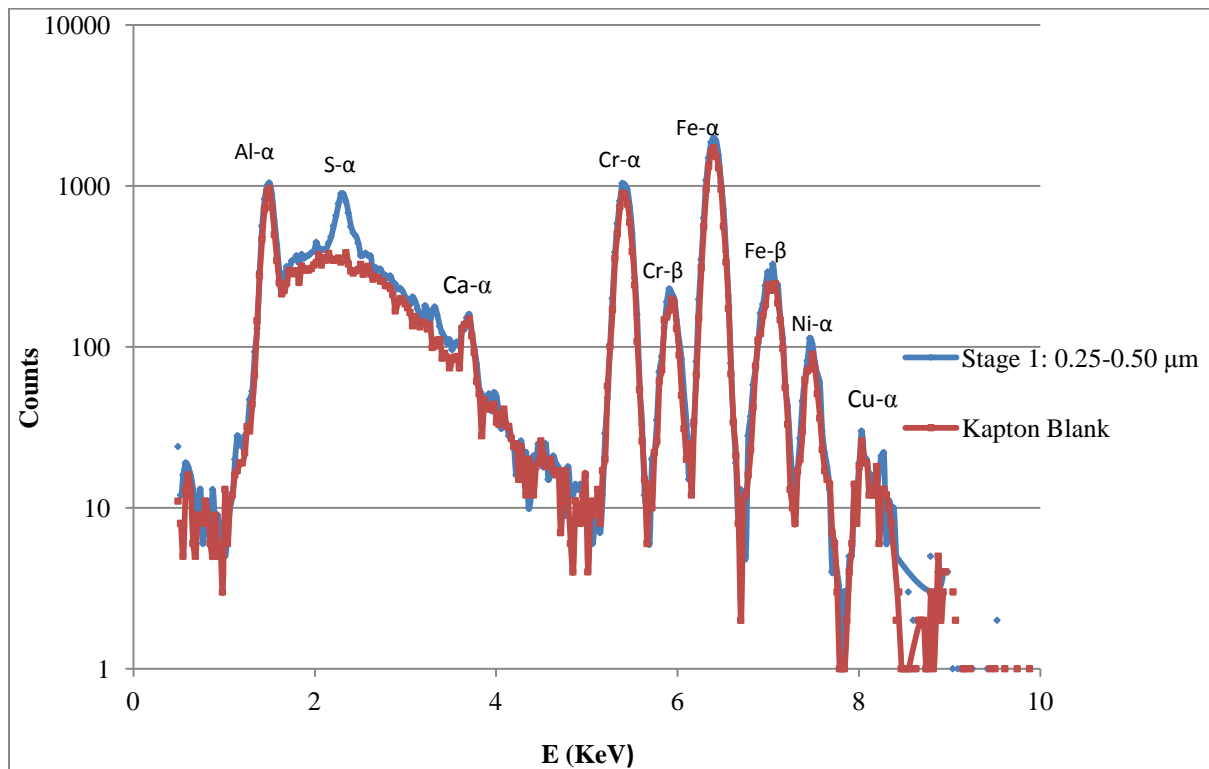


**Figure 14**. September 2012 stage 1 (PM 0.25-0.50): X-ray energy vs. counts (log scale).

We used a table of characteristic X-ray energies to match peaks to elements and transition types. . As seen above, Bremsstrahlung background radiation is evident in the 1 – 5 keV range, and sulfur, chromium, and iron appear the most prevalent (at least for this impaction stage). It should be noted that there may be more elements in the sample than just the ones corresponding to clear peaks in the figures; the GUPIX program is designed to find elements that may be missed by human inspection of the X-ray energy spectrum. We therefore used GUPIX to find all elements present and corresponding concentrations (mass per unit area), and we subtracted concentrations found for the blank kapton foil. July results are represented below in Table 4 and Figure 15, while September results are seen in Table 5 and Figure 16.[7] All uncertainty propagations may be found in Appendix 2.

| | | $C_A + \Delta C_A$ (ng/cm$^2$) | | | | |
|---|---|---|---|---|---|---|
| Z | Element | Stage 1: 0.25 - 0.50 μm | Stage 2: 0.5 – 1.0 μm | Stage 3: 1 - 2 μm | Stage 4: 2 - 4 μm | Stage 5: 4 - 8 μm |
| 13 | Al | <LOD[8] | <LOD | 2300 ± 200 | 100 ± 100 | 100 ± 100 |
| 14 | Si | 20 ± 40 | 170 ± 40 | 2720 ± 80 | 1140 ± 50 | 730 ± 50 |
| 15 | P | 10 ± 30 | 50 ± 30 | 600 ± 40 | 860 ± 30 | 200 ± 20 |
| 16 | S | 1280 ± 40 | 1910 ± 30 | 3190 ± 50 | 590 ± 20 | 130 ± 20 |
| 19 | K | 150 ± 10 | 170 ± 10 | 2310 ± 30 | 2520 ± 30 | 510 ± 20 |
| 20 | Ca | <LOD | 40 ± 20 | 2510 ± 40 | 1840 ± 30 | 1430 ± 30 |
| 24 | Cr | 500 ± 200 | 100 ± 200 | 1800 ± 200 | <LOD | 500 ± 200 |
| 25 | Mn | 100 ± 100 | 100 ± 100 | 300 ± 100 | 100 ± 100 | 200 ± 100 |
| 26 | Fe | 1700 ± 200 | 1300 ± 200 | 7300 ± 200 | 200 ± 200 | 1100 ± 200 |
| 27 | Co | 100 ± 100 | 10 ± 90 | 400 ± 100 | 100 ± 100 | 100 ± 100 |
| 28 | Ni | 100 ± 90 | 50 ± 90 | 400 ± 100 | <LOD | 20 ± 90 |
| 29 | Cu | 60 ± 70 | 170 ± 70 | 260 ± 70 | 60 ± 60 | <LOD |

**Table 4**. July 2012: Elemental concentrations (ng/cm$^2$).

[7] Note that in Figures 15-18, some error bars that rise significantly above the data bar, but not downward at all, indicate concentrations with errors greater than the concentration itself; this is because the graphing software does not show downward error bars that extend below the x-axis.
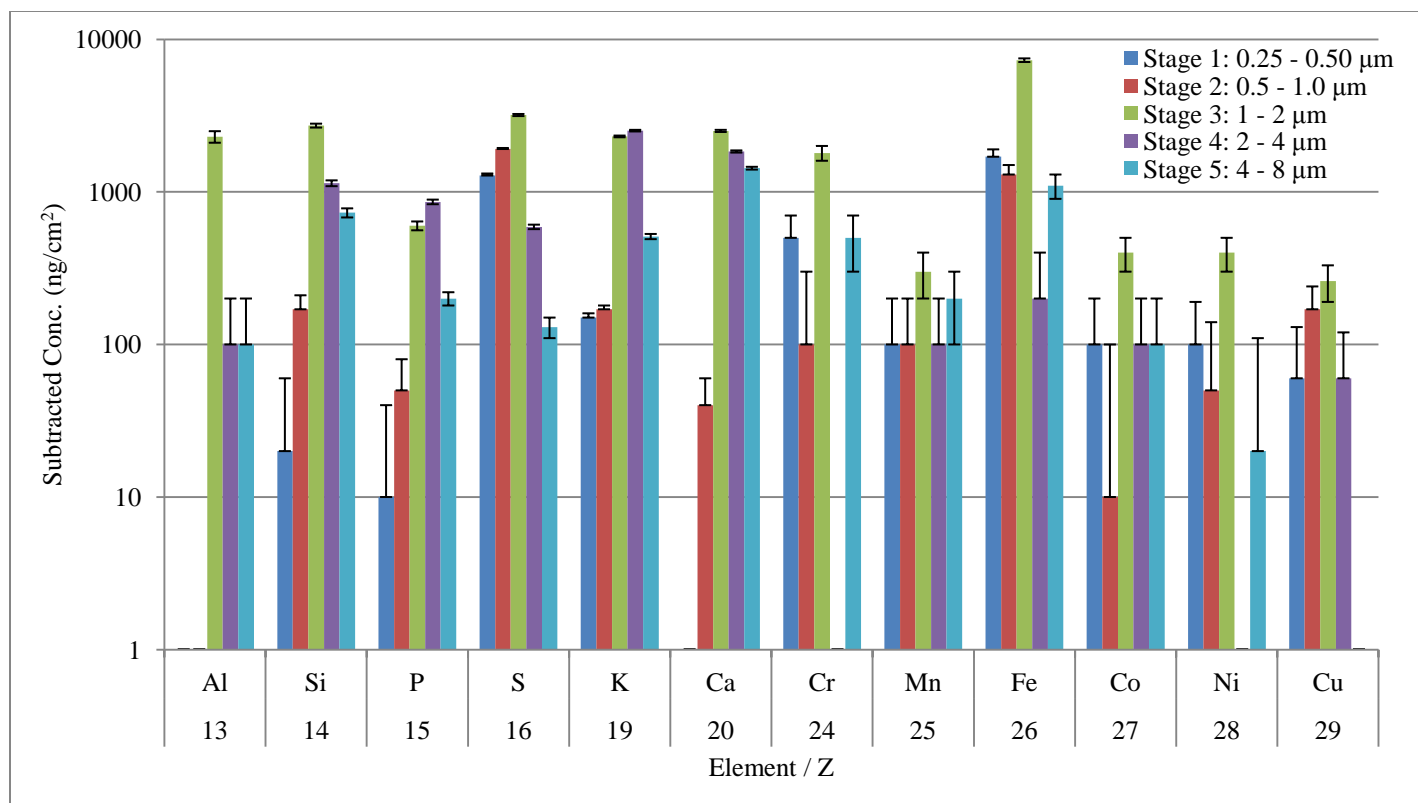[8] <LOD indicates concentrations that were below levels of detection.

**Figure 15**. July 2012: Elemental concentrations (ng/cm$^2$) corresponding to Table 4. All values were determined computationally by GUPIX.

| | | $C_A + \Delta C_A$ (ng/cm$^2$) | | | | |
|---|---|---|---|---|---|---|
| Z | Element | Stage 1: 0.25-0.50 μm | Stage 2: 0.5-1.0 μm | Stage 3: 1-2 μm | Stage 4: 2-4 μm | Stage 5: 4-8 μm |
| 13 | Al | 300 ± 100 | 500 ± 100 | 400 ± 100 | <LOD | 100 ± 100 |
| 14 | Si | <LOD | 20 ± 40 | 110 ± 30 | 100 ± 30 | 60 ± 30 |
| 15 | P | <LOD | <LOD | 60 ± 20 | 330 ± 30 | 150 ± 20 |
| 16 | S | 330 ± 20 | 2160 ± 60 | 990 ± 30 | 300 ± 20 | 90 ± 20 |
| 19 | K | 30 ± 10 | 90 ± 10 | 200 ± 10 | 990 ± 20 | 370 ± 20 |
| 20 | Ca | <LOD | 30 ± 20 | 30 ± 20 | 110 ± 20 | 60 ± 20 |
| 24 | Cr | 400 ± 200 | 700 ± 200 | 600 ± 200 | <LOD | <LOD |
| 25 | Mn | <LOD | <LOD | <LOD | <LOD | <LOD |
| 26 | Fe | 1500 ± 200 | 2200 ± 300 | 1900 ± 200 | <LOD | <LOD |
| 27 | Co | 100 ± 100 | 200 ± 100 | 200 ± 100 | 10 ± 90 | <LOD |
| 28 | Ni | 170 ± 90 | 300 ± 100 | 210 ± 90 | <LOD | 70 ± 80 |
| 29 | Cu | 10 ± 70 | 140 ± 80 | <LOD | 50 ± 70 | <LOD |

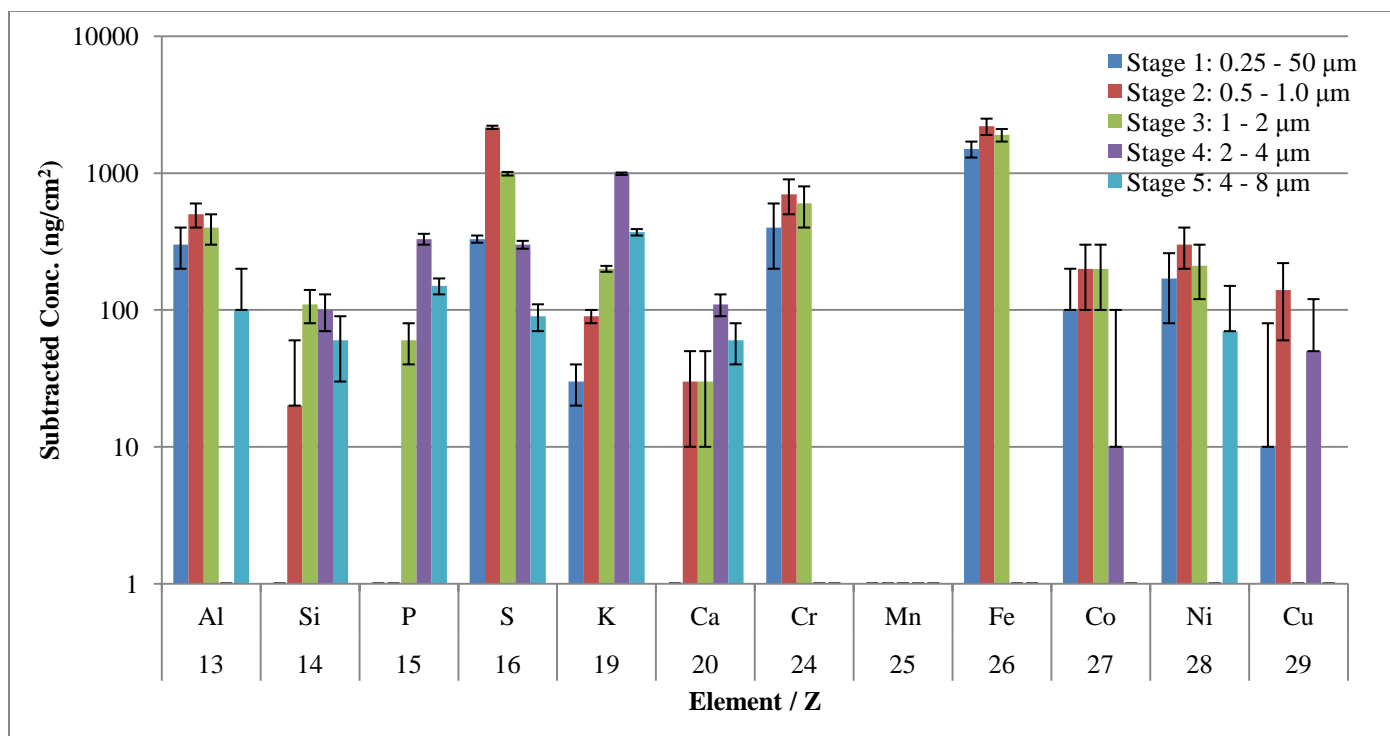**Table 5**. September 2012: Elemental concentrations (ng/cm$^2$).

**Figure 16**. September 2012: Elemental concentrations (ng/cm$^2$) corresponding to Table 5. All values were determined computationally by GUPIX.

As seen in the tables and figures above, our highest elemental concentrations were found for iron and sulfur. In July, iron and sulfur particles were most prevalent in the 1 – 2 μm range (stage 3), with concentrations of (7300 ± 200) ng/cm$^2$ and (3190 ± 50) ng/cm$^2$, respectively. In September, iron and sulfur particles were most prevalent in the 0.5 – 1.0 μm range (stage 2), with concentrations of (2220 ± 300) ng/cm$^2$ and (2160 ± 60) ng/cm$^2$, respectively. Phosphorus, chromium, and aluminum were also found in significant quantities in both months, while silicon and calcium had greater concentrations relative to other elements in July than in September. Cobalt, nickel, and copper were found in small amounts (0 – 300 ng/cm$^2$) for both months as well. We found manganese in low concentrations with high uncertainties in July, but we saw no manganese in September. Overall, elemental concentrations were much greater in July than in September. We substituted the values from

19

Table 4 and Table 5 into Eq. 10 to convert the concentrations from mass per unit area to mass per unit volume.  Our final results are seen below in Table 6 and Figure 17 (July), and Table 7 and Figure 18 (September).

| | | $C_v + \Delta C_v$ (ng/m³) | | | | |
|---|---|---|---|---|---|---|
| Z | Element | Stage 1: 0.25 - 0.50 μm | Stage 2: 0.5 - 1.0 μm | Stage 3: 1 - 2 μm | Stage 4: 2 - 4 μm | Stage 5: 4 - 8 μm |
| 13 | Al | <LOD | <LOD | 41 ± 9 | 6 ± 1 | 11 ± 3 |
| 14 | Si | 0.17 ± 0.04 | 2.9 ± 0.7 | 50 ± 10 | 80 ± 20 | 80 ± 20 |
| 15 | P | 0.11 ± 0.03 | 0.8 ± 0.2 | 10 ± 2 | 60 ± 10 | 22 ± 5 |
| 16 | S | 11 ± 3 | 33 ± 8 | 60 ± 10 | 41 ± 9 | 15 ± 4 |
| 19 | K | 1.3 ± 0.3 | 2.9 ± 0.7 | 40 ± 9 | 170 ± 40 | 60 ± 10 |
| 20 | Ca | <LOD | 0.7 ± 0.2 | 40 ± 10 | 130 ± 30 | 160 ± 40 |
| 24 | Cr | 4 ± 1 | 1.6 ± 0.4 | 32 ± 7 | <LOD | 50 ± 10 |
| 25 | Mn | 1.1 ± 0.2 | 1.6 ± 0.4 | 6 ± 1 | 8 ± 2 | 20 ± 5 |
| 26 | Fe | 15 ± 3 | 22 ± 5 | 130 ± 30 | 11 ± 3 | 130 ± 30 |
| 27 | Co | 0.9 ± 0.2 | 0.12 ± 0.03 | 7 ± 2 | 7 ± 2 | 17 ± 4 |
| 28 | Ni | 0.9 ± 0.2 | 0.8 ± 0.2 | 7 ± 2 | <LOD | 2.1 ± 0.5 |
| 29 | Cu | 0.5 ± 0.1 | 2.9 ± 0.7 | 5 ± 1 | 4 ± 1 | 0.23 ± 0.06 |

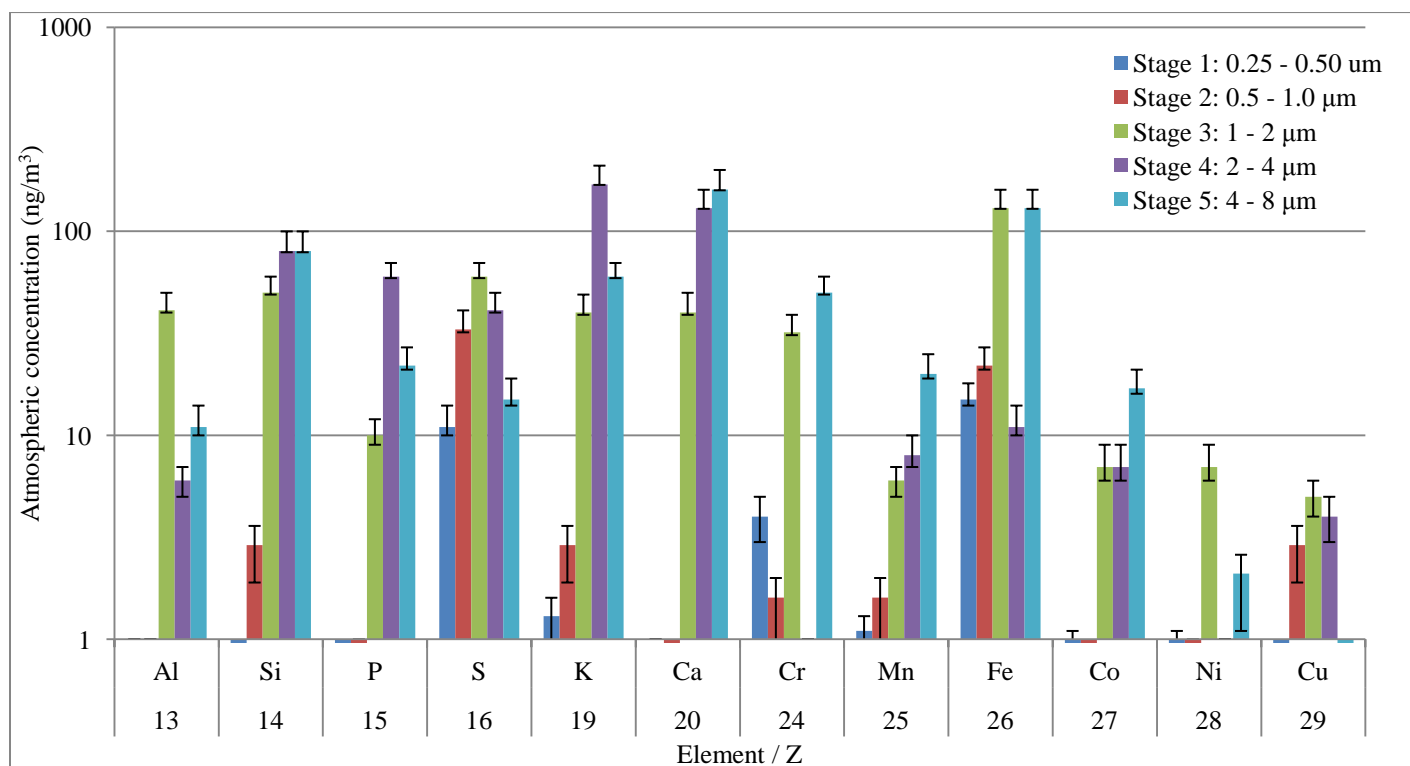**Table 6**. July 2012: Elemental concentrations (ng/m³)



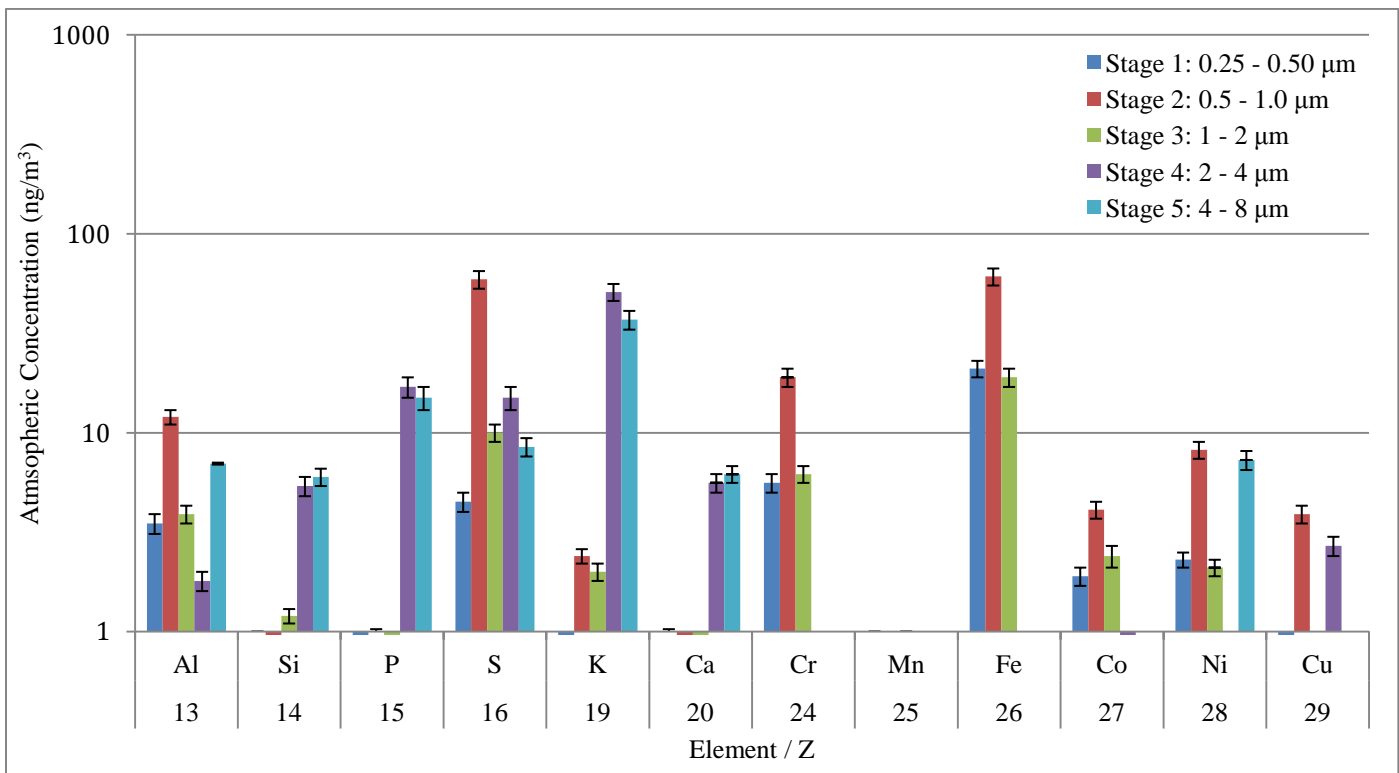**Figure 17**. July 2012: Elemental concentrations (ng/m³) corresponding to Table 6.  All values were calculated using Table 4 and Eq. 10.

| | | $C_v + \Delta C_v$ (ng/m³) | | | | |
|---|---|---|---|---|---|---|
| Z | Element | Stage 1: 0.25 - 0.50 μm | Stage 2: 0.5 - 1.0 μm | Stage 3: 1 - 2 μm | Stage 4: 2 - 4 μm | Stage 5: 4 - 8 μm |
| 13 | Al | 3.5 ± 0.4 | 12 ± 1 | 3.9 ± 0.4 | 1.8 ± 0.2 | 7.0 ± 0.8 |
| 14 | Si | <LOD | 0.42 ± 0.06 | 1.2 ± 0.1 | 5.4 ± 0.6 | 6.0 ± 0.6 |
| 15 | P | 0.01 ± 0.02 | <LOD | 0.63 ± 0.07 | 17 ± 2 | 15 ± 2 |
| 16 | S | 4.5 ± 0.5 | 59 ± 6 | 10 ± 1 | 15 ± 2 | 8.5 ± 0.9 |
| 19 | K | 0.40 ± 0.04 | 2.4 ± 0.2 | 2.0 ± 0.2 | 51 ± 5 | 37 ± 4 |
| 20 | Ca | <LOD | 0.81 ± 0.08 | 0.30 ± 0.03 | 5.6 ± 0.6 | 6.2 ± 0.6 |
| 24 | Cr | 5.6 ± 0.6 | 19 ± 2 | 6.2 ± 0.6 | <LOD | <LOD |
| 25 | Mn | <LOD | <LOD | <LOD | <LOD | <LOD |
| 26 | Fe | 21 ± 2 | 61 ± 6 | 19 ± 2 | <LOD | <LOD |
| 27 | Co | 1.9 ± 0.2 | 4.1 ± 0.4 | 2.4 ± 0.3 | 0.5 ± 0.1 | <LOD |
| 28 | Ni | 2.3 ± 0.2 | 8.2 ± 0.8 | 2.1 ± 0.2 | <LOD | 7.3 ± 0.8 |
| 29 | Cu | 0.10 ± 0.08 | 3.9 ± 0.4 | <LOD | 2.7 ± 0.3 | <LOD |

**Table 7**. September 2012: Elemental concentrations (ng/m³).



**Figure 18**. September 2012: Elemental concentrations (ng/m³) corresponding to Table 7. All values were calculated using Table 5 and Eq. 10.

As seen above, the relative difference in areal concentrations between elements is similar to the relative difference in mass-per-unit volume concentrations between elements. However, because the area of the particulate matter on the kapton foil changed depending on the stage of impaction, the prevalence of some elements varied. For instance, potassium particles with diameters in the 2 – 4 μm range and calcium particles with diameters in the 4 – 8 μm range now dominated for the July air samples, with concentrations of (170 ± 40) and (160 ± 40) ng/m$^3$, respectively. However, the most noticeable difference between the two months' results for volume concentrations is the amount of particulate matter in the air. Either the difference in concentrations between July and September is indicative of very different elemental compositions for the air two months apart, or it is the result of a common systematic error. We now address this question.

**Discussion**

Notwithstanding the specific elemental concentrations that we have found, the most noticeable feature of our results is the constant shift in concentration values from July to September. By simple inspection of Figures 15 and 16, and Figures 17 and 18, we observe that the elemental concentrations (both $C_A$ and $C_V$) are approximately 2-3 times higher in July than in September. This does not appear to be an effect of changes in atmospheric conditions from July to September, as pressure and temperature did not vary much between air samplings. Had we observed a significant change in pressure in particular, this may have signified a strong storm capable of temporarily altering the composition of atmospheric aerosols. However, this was not the case: while the impactor was running in July, the mean temperature was (24 ± 5) °C and the mean pressure was (760.0 ± 0.9) mm Hg; in September, the mean temperature was

(20 ± 3) ℃ and the mean pressure (757.3 ± 0.9) mm Hg.  Neither can the disparity in concentrations be accounted for by flow rate or time duration, both of which were kept reasonably constant for the two runs.  Furthermore, as seen in Figure 12 and Table 3, the areas of the particulate deposits varied little.   When considering the relation given by Eq. 10, it is clear then that the significant difference in results between July and September is due solely to the GUPIX concentrations (mass per unit area).

The question then remains whether these concentrations were *actually* different between July and September, i.e., despite similar atmospheric conditions, time duration, flow rate, and area of impaction, there were still more particles on the kapton foils in July than in September, or whether this variance was the result of an error in the PIXE analysis.  We begin to answer this by first analyzing H, the calibration value obtained from the standards and used to calculate concentrations in GUPIX.  In our plot of Z vs. H (Figure 11), there is a noticeable shift down from the July to September values.  For consistency – and because we originally did not expect there to be any actual change in the accelerator procedure – we averaged all H's and used one value for both months.  However, we erred in this judgment, as we later found out that the shifts in H represented real changes in the accelerator procedure (discussed in detail below, p. 26-27), and so this caused our single H value to come out too low for July and too high for September.[9]  According to the relation seen in Eq. 8, where H is in the denominator, this inflated the concentrations in July and lowered the concentrations in September, in line with our results.

---

[9] In attempting to represent both months equally, we also erred in using the H value obtained from germanium, as this was not used as a standard in July.

Research done by Professor Michael Vineyard further supports this conclusion.

Professor Vineyard re-analyzed the September data with GeoPIXE [18], a quantitative PIXE

imaging and analysis software, using an H value obtained from only the copper and germanium

standards for that month.  Professor Vineyard's GeoPIXE results for the September

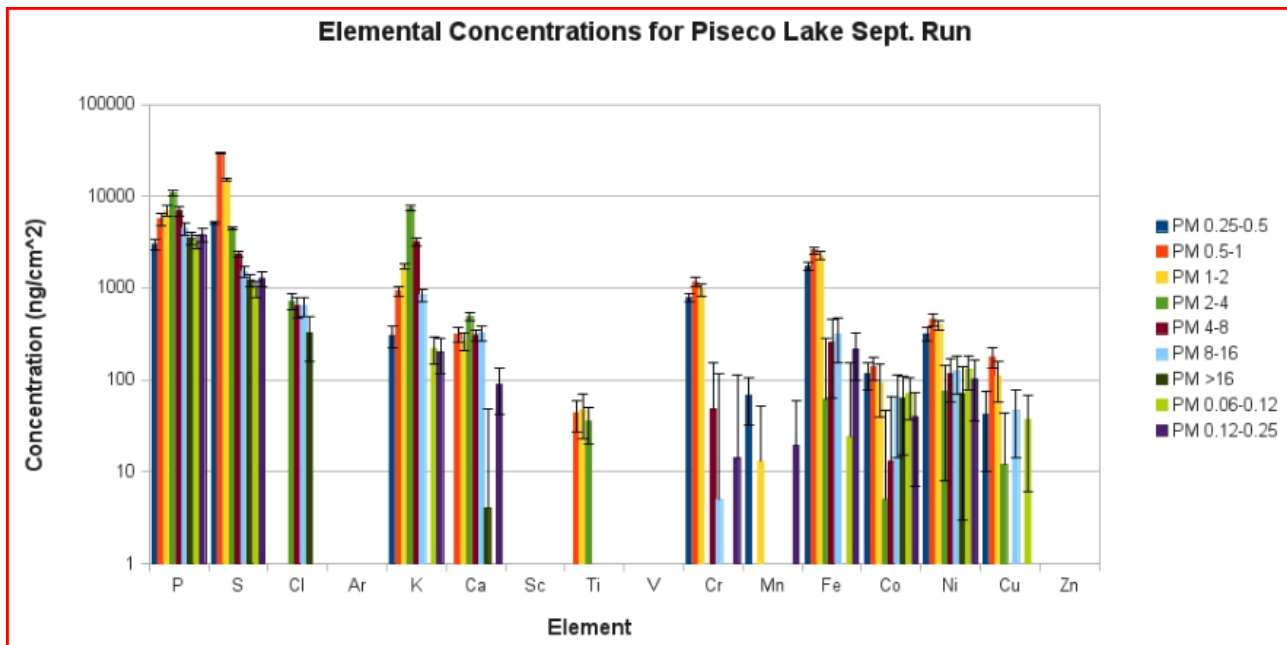concentrations (mass/area) are seen below in Figure 19.



**Figure 19**. Professor Vineyard's results: September concentrations with H = 0.0021.  This H
value is smaller than the one used in our study (H = 0.002483) by a 15% difference.

As seen in Figure 19, over twenty different concentrations are now between 1,000 and

10,000 ng/cm$^2$, whereas before (Figure 16) only 4 concentrations in total broke 1000 ng/cm$^2$.

However, these results mostly support our findings of relative concentrations.  Both sets of

results are consistent in showing high concentrations of iron, sulfur, potassium, phosphorus,

and chromium; moderate levels of calcium, cobalt, nickel, and copper; trace amounts of

manganese; and no presence of argon, scandium, vanadium, or zinc.  Professor Vineyard's

results also show small amounts of chlorine and titanium, which we detected in very small

quantities in only a few impaction foils, and therefore did not include.  Figure 19 also displays

particulate matter in impaction stages 6, 7, L1, and L2.  While some particulate matter may be

seen in these stages, it is mostly in very low quantities, and thus does not contradict our basic

findings.

While we have now established that the variance in H values seen in Figure 11 is

representative of an actual physical change, we now turn our attention to the nature and cause

of this change.  Following the September data runs, we tested the accelerator with and without

target material in the chamber.  The resulting proton beam, which spreads drastically up

hitting on the target, is seen below in Figure 20.  Although we do not possess similar figures for

the July research or earlier, Equation 8 would suggest that our higher July concentrations

indicate even less charge detected (i.e., more beam spread) in July than in September.
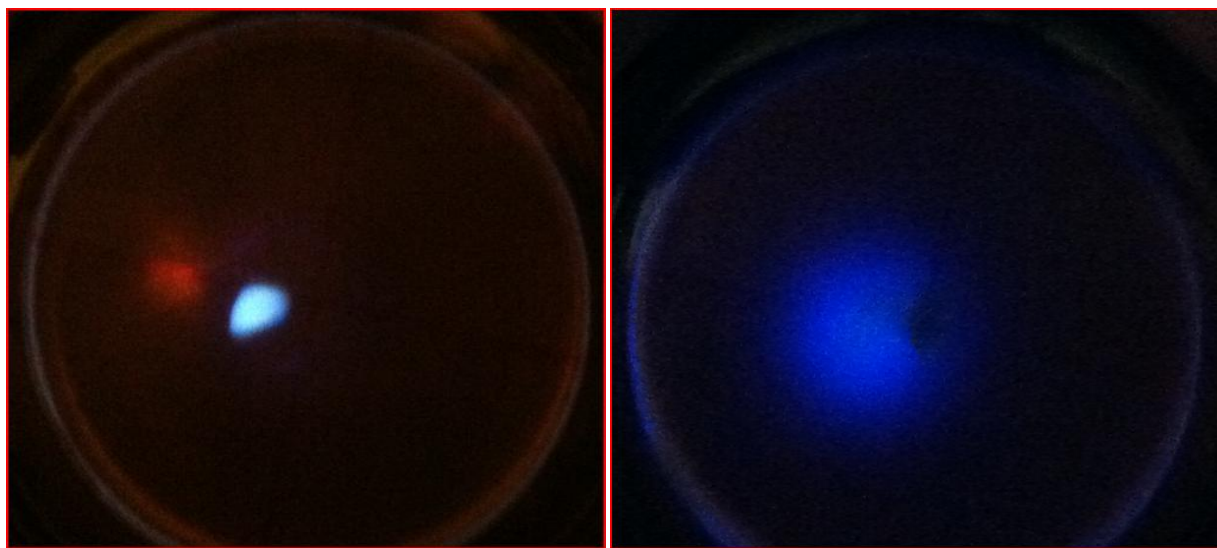


**Figure 20**. Ion beam without target material (left) and after passing through plastic scintillator
(right).

The width of the spread in the beam is greater than the width of our current Faraday

cup aperture (seen below in Figure 21), causing two adverse effects.  First, it is likely that the

beam now interacts with aluminum in the cup and the cup's stainless steel ring. Thus our data is contaminated by aluminum and elements found in stainless steel, such as iron, chromium, and nickel. Since we assume that the level of contamination is roughly constant for the kapton foil before and after impaction, we mostly overcome this problem when we subtract the blank kapton concentrations from the concentrations of the kapton with aerosols impacted. However, our calibration is still skewed from contaminants that are the same as standards used to calculate H. For instance, we see in Figure 11 that H is significantly greater for iron than for the other standards. This follows from Eq. 9, since the iron concentrations will be higher due to contamination from the Faraday aperture.
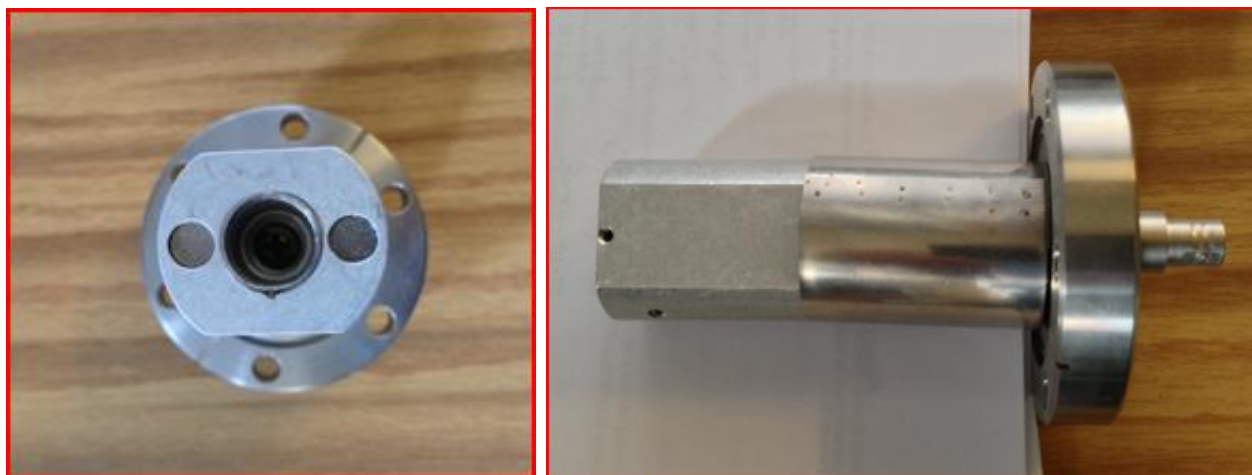


**Figure 21**. Left: cross-sectional view of the Faraday cup aperture. Right: profile of the Faraday cup disconnected from the scattering chamber. The ion beam would enter from the left.

The second adverse effect caused by the beam spreading is one of charge integration. This problem can be fixed by either finding out how to reduce the spread, or, more easily, by constructing a new faraday cup with an aperture that is larger and closer to the target. The latter process is currently underway. For now, this effect means that elemental concentrations (both $C_A$ and $C_V$) are inaccurate across the spectrum for September and July. Therefore, our

research may be used to draw conclusions as to what elements are in the air at Piseco Lake,

and their relative quantities, but absolute quantitative results are fundamentally flawed.

Despite the systematic errors stemming from our inaccurate H value and the beam

spreading, by considering the relative quantities, we can still use emission profiles to speculate

as to the source of particulate matter in the Adirondacks.  Although we do not possess data

specific to the Adirondack region or to the Mid-west of the United States, general pollution

sources such as motor vehicle and coal burning companies have been extensively profiled as

part of various international projects.  In one 1996 research effort, David Cohen, Grahame

Bailey, and Ramesh Kondepudi used PIXE to fingerprint atmospheric aerosol fine particle

pollution in Australia.[10]  The profiles they used are seen below in Figure 22.  We note that

while deposits on stages 4 and 5 of the cascade impactor are considered "inhalable coarse

particles" (2.5µm ≤ diameter ≤ 10 µm), the more dangerous "fine particles" (diameter ≤ 2.5µm)

are mostly found in stages 1 – 3.   However, the U.S. Environmental Protection Agency (EPA)

considers all particles with diameter less than ten microns potentially hazardous due to their

ability to pass through the throat into the lungs [22].

---

[10] For some other similar efforts, see Ancelet et al [19] and Davy et al [20].
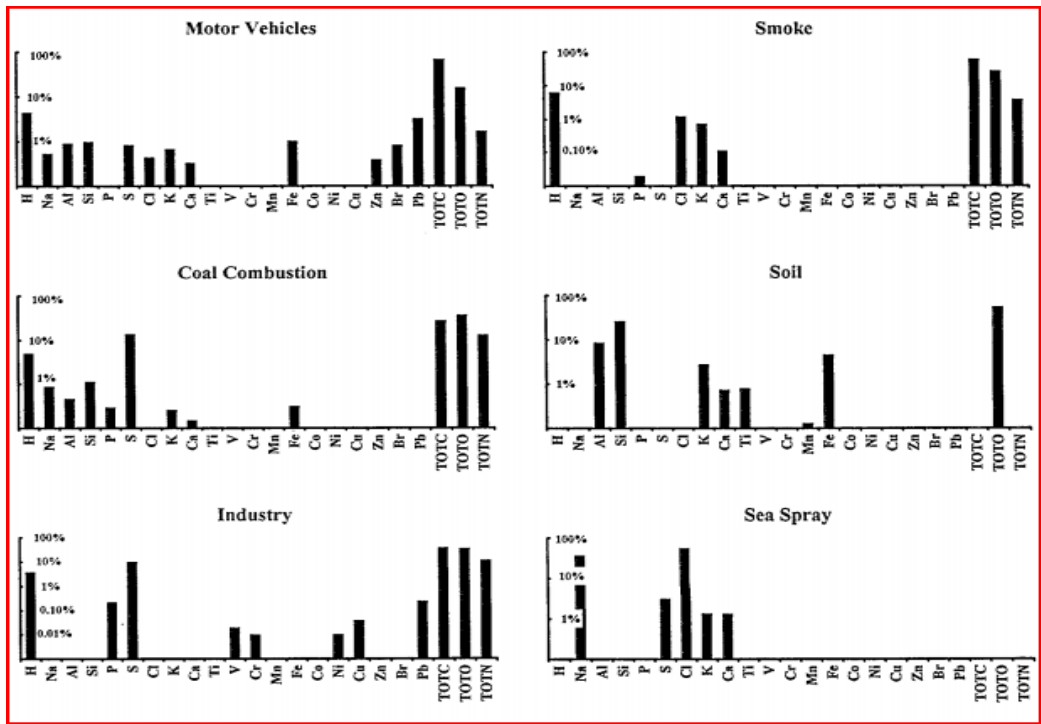
**Figure 22**. Fine particle pollutant profiles for six Australian sources [21].

Upon inspection of Figure 22, the most likely culprit for pollution in the Adirondacks is coal combustion. This profile shares many features of Figures 15 – 18. For instance, coal combustion does not release vanadium, zinc, bromine, or lead, but it does emit significant quantities of iron, calcium, potassium, phosphorus, silicon, aluminum, and high levels of sulfur. In fact, there is nothing that coal combustion produces that we did not observe in our research (sodium borders on what is too light for PIXE to detect, and hydrogen is too light for detection). This connection is strengthened by the fact that the majority of U.S. coal reserves are located in the Midwest and Appalachian Mountains, as seen below in Figure 23. We recognize that all coal burning sites are not necessarily located in the same region as coal reserves; however, we assume for the purposes of the discussion that the two regions are similar.

**Figure 23**. United States Geological Survey (USGS) map of coal reserves. The large Illinois and Appalachian basins are located southwest of Piseco Lake [23].

As seen in Figure 23, the Illinois and Appalachian basins are positioned such that west-to-east weather systems could carry particulate matter from coal combustion a relatively short distance to the Adirondack region of New York State. Coal combustion, however, does not account for the concentrations of chromium, cobalt, nickel, and copper that we observed; and it also does not explain the prevalence of iron in our results. In fact, none of the profiles in Figure 22 emit noticeable levels of cobalt. Emissions from industry could explain the presence of copper, nickel, and chromium, but there should be some explanation for why we do not observe any vanadium or lead. Adirondack soil may be the cause of high levels of iron and trace amounts of manganese, but the existence of titanium, seen by Professor Vineyard (Figure 19) and in Appendix 1, is also unaccounted for by the Figure 22 profiles.

Other ion beam analysis (IBA) techniques may be used to supplement our study. These include proton induced gamma ray emission (PIGE) spectrometry, proton elastic scattering analysis (PESA), and Rutherford backscattering spectrometry (RBS). While we will not

provide an in depth discussion of how these techniques work[11], it suffices to say that the same

proton beam for PIXE can be used for PIGE and PESA; but whereas we collected data from X-

rays for PIXE, these methods use data from gamma rays and scattered protons, respectively.

RBS differs from other IBA techniques as it does not use a beam of protons, but a beam of alpha

particles that scatter off of the target.  The advantage of using different techniques is mainly

due to the range of elements that can be detected.  While PIXE is generally very good at

determining concentrations of elements from aluminum through uranium (and sometimes

sodium and magnesium), PIGE can detect lithium, boron, fluorine, sodium, and magnesium

(among others); PESA can detect hydrogen; and RBS can detect nitrogen, carbon, oxygen, and

other elements [24].  Since metals are usually considered more harmful as particulate matter

in the air, PIXE is generally considered the best IBA technique for an environmental study.

However, a more complete picture can be formed by using multiple methods.

We hope to accomplish three main goals in our future research.  First, we hope that by

using a Faraday cup that captures all of the charge from the ion beam, our calibrations will be

better and therefore our relative elemental concentrations will be more accurate.  Second, we

hope to extend our sampling to different times throughout the year, to find whether elemental

compositions vary significantly with seasonal changes.  Finally, and most importantly, we

believe that the new Faraday cup will enable us to determine credible concentrations in mass

per unit volume.  By accomplishing the third goal in particular, we may begin to quantify the

environmental and human impact from particulate matter in atmospheric aerosols of the

Adirondacks.

---

[11] For a more detailed overview of these alternative IBA techniques, see [24-25].  Some elemental
analysis studies employ one or more of these methods, e.g., Cohen et al [21].

**Works Cited**

[1]     Driscoll, C. T., K. M. Driscoll, K. M. Roy, and M. J. Mitchell. 2003.  "Chemical Response of Lakes in the Adirondack Region of New York to Declines in Acidic deposition." *Environ. Sci. Technol.* 37(10): 2036-2042.

[2]     Sullivan, T. J. 2000. *Aquatic effects of acid deposition.* Boca Raton: Lewis Publishing.

[3]     Sullivan, T. J., I. J. Fernandez, A. T. Herlihy, C. T. Driscoll, T. C. McDonnell, N. A. Nowicki, K. U. Snyder, and J. W. Sutherland. 2006.  "Acid-base Characteristics of Soils in the Adirondack Mountains, New York." *Soil Sci. Soc. Am. J.* 70: 141-142.

[4]     New York State Department of Environmental Conservation. 2013. "New Yorks [sic] Acid Deposition Monitoring Network." Accessed March 3. http://www.dec.ny.gov/chemical/24754.html.

[5]     H.G. J. Moseley. 1913-1914. "The High Frequency Spectra of the Elements." *Phil. Mag.* 26: 1024.

[6]     Johansson, S. A. E., J. Campbell, and K. G. Malmqvist, eds. 1995. *Particle Induced X-Ray Emission Spectrometry (PIXE)*. New York: John Wiley & Sons, Inc.

[7]     Institut für Kernphysik, Universität zu Köln. "PIXE Experimental Set-up in Cologne, 2003." Accessed March 3. http://www.ikp.uni-koeln.de/research/pixe/bildchen/x_ray_transitions.jpg. Citing Johansson, S. A. E. and J. L. Campbell. 1988. *PIXE: A Novel Technique for Elemental Analysis*. New York: John Wiley & Sons.

[8]     Haigh, C. W. 1995.  "Moseley's Work on X-rays and Atomic Number." *J. Chem. Educ.* 72(11): 1012-1014.

[9]     Naqvi, K. R. 1996. "The physical (in)significance of Moseley's screening parameter." *Am. J. Phys.* 64(10): 1332.

[10]    PIXE International Corp. 2013. "PIXE Cascade Impactors." Accessed March 3. http://pixeintl.com/Impactor.asp

[11]    University of Guelph. 2007.  "The GUPIXWIN Manual and User-Guide, Ver. 2. 1."

[12]    Labrake, S. M. 2012. "Physics 300 Laboratory Manual." Accessed March 3. http://minerva.union.edu/labrakes/Phy300_Laboratory_Manual.pdf.

[13]    Labrake, S. M. 2011. "The Union College Ion Beam Analysis Lab." Accessed March 3. http://minerva.union.edu/labrakes/accelerator.htm.

[14]    National Electrostatics Corporation. 2001. "Charging System." Accessed March 3. http://www.pelletron.com/charging.htm.

[15]    Labrake, S. M. 2012. "PIXE Physics 300 Lecture Notes."

[16]    University of Guelph. 2013. "GUPIX: the versatile PIXE spectrum fitting software." Accessed March 3. http://pixe.physics.uoguelph.ca/gupix/main.

[17]    Weather Underground. 2013. "Historical Weather." Accessed March 3. http://www.wunderground.com/history.

[18]    Nuclear Microprobe Analysis. 2011. "GeoPIXE: Quantitative PIXE Imaging and Analysis Software." Accessed March 3. http://www.nmp.csiro.au/GeoPIXE.html.

[19]    Ancelet, T. P. K. Davy, T. Mitchell, W. J. Trompetter, A. Markwitz, and D. C. Weatherburn. 2012. "Identification of Particulate Matter Sources on an Hourly Time-Scale in a Wood Burning Community." *Environ. Sci. Technol.* 46: 4767-4774.

[20]    Davy, P. K., G. Gunchin, A. Markwitz, W. J. Trompetter, B. J. Barry, D. Shagjjamba, and S. Lodoysamba. 2011. "Air particulate matter pollution in Ulaanbaatar, Mongolia: determination of composition, source contributions and source locations." *Atmospheric Pollution Research* 2: 126-137.

[21]    Cohen, D. D., G. M. Bailey, R. Kondepudi. 1996.  "Elemental analysis by PIXE and other IBA techniques and their application to source fingerprinting of atmospheric fine particle pollution." *Nuc. Instr. and Meth. in Phys. Res. B* 109/110: 218-226.

[22]    United States Environmental Protection Agency. 2013. "Particulate Matter (PM)." Accessed March 3. http://www.epa.gov/pm.

[23]    United States Geological Survey, United States Department of the Interior. 2012. "Energy Resources Program." Accessed March 3. http://energy.usgs.gov/Coal/AssessmentsandData/CoalAssessments.aspx.

[24]    Department of Neutron Physics, Nuclear Physics Institute, The Academy of Sciences of the Czech Republic. 2010. "PIXE, PIGE, and PESA." Accessed March 3. http://neutron.ujf.cas.cz/en/lnam/item/81-pixe

[25]    Labrake, S. M. 2012. "RBS Physics 300 Lecture Notes."
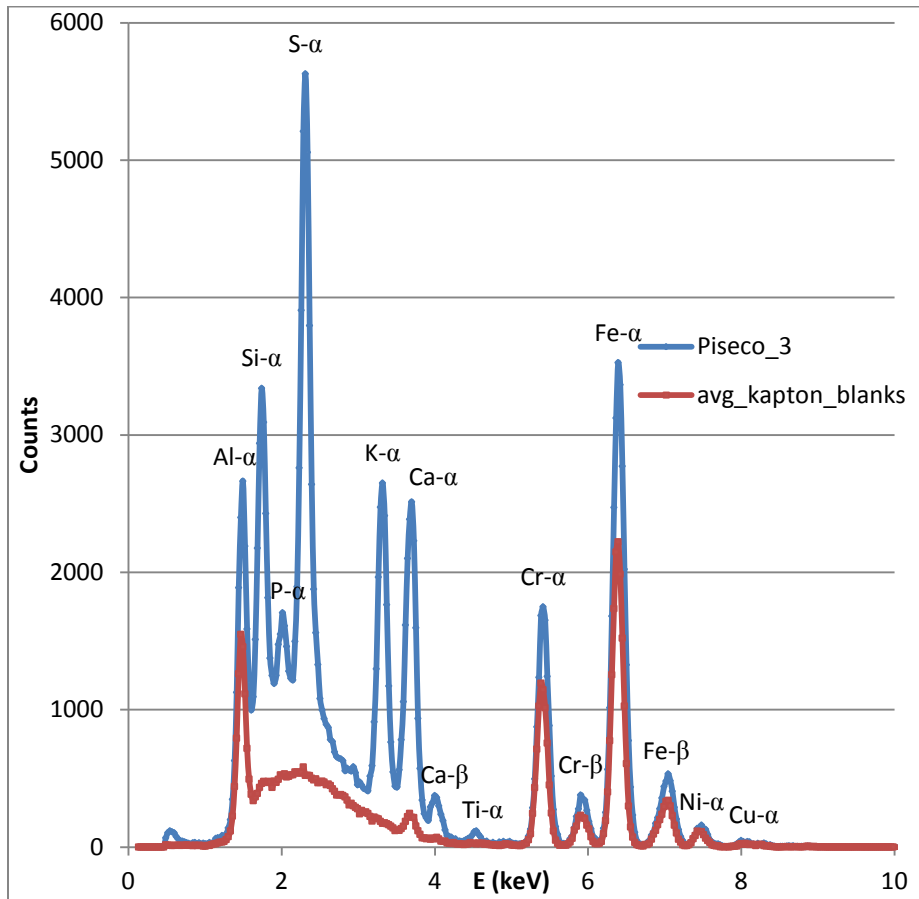
# Appendix 1

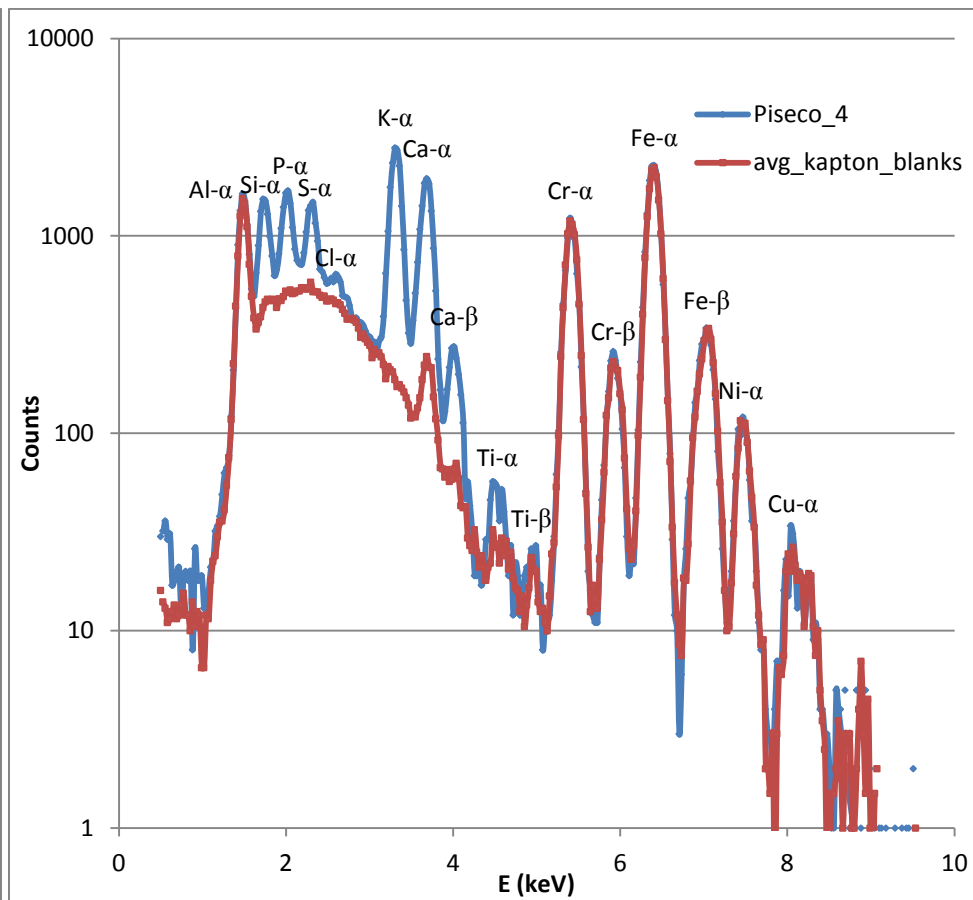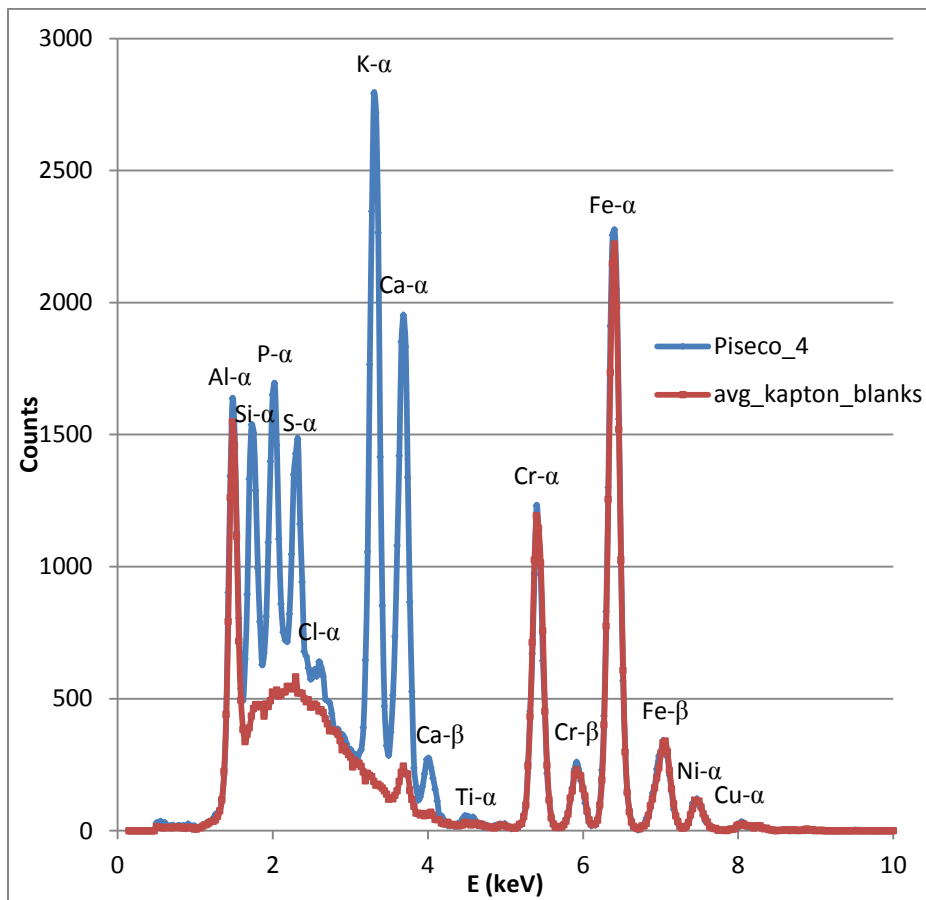GUPIX X-ray Spectra for July and September Aerosols, Impaction Stages 1 - 5
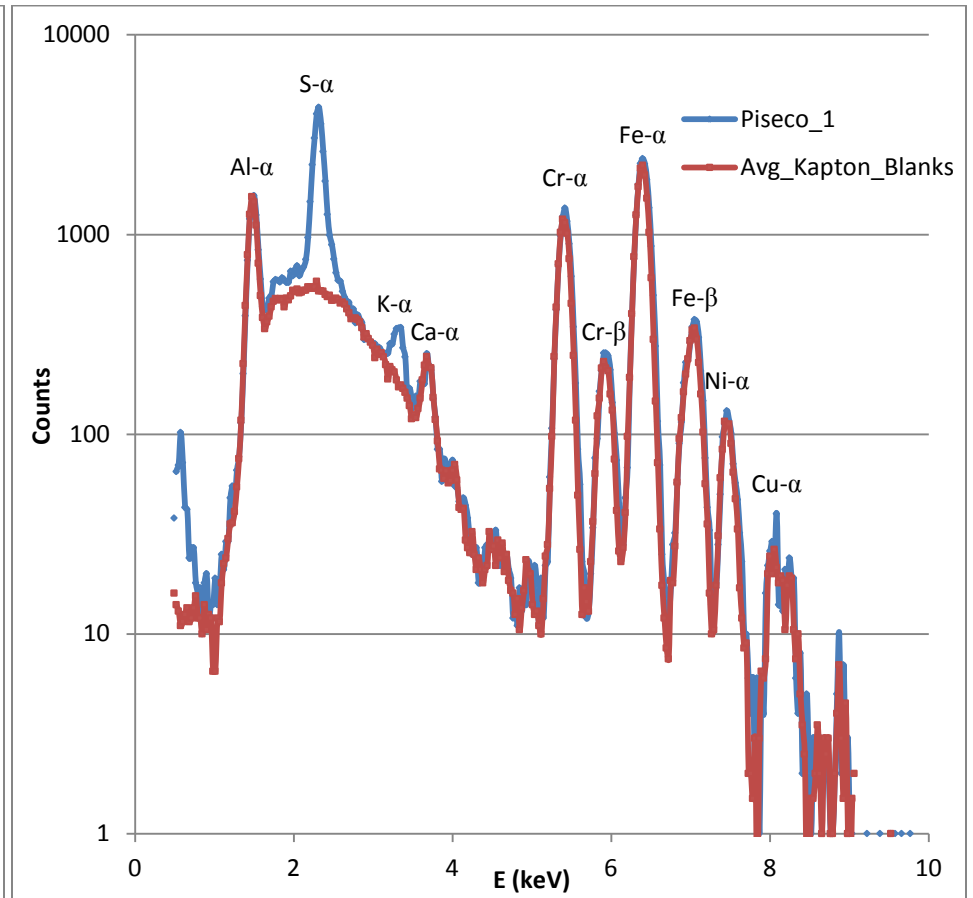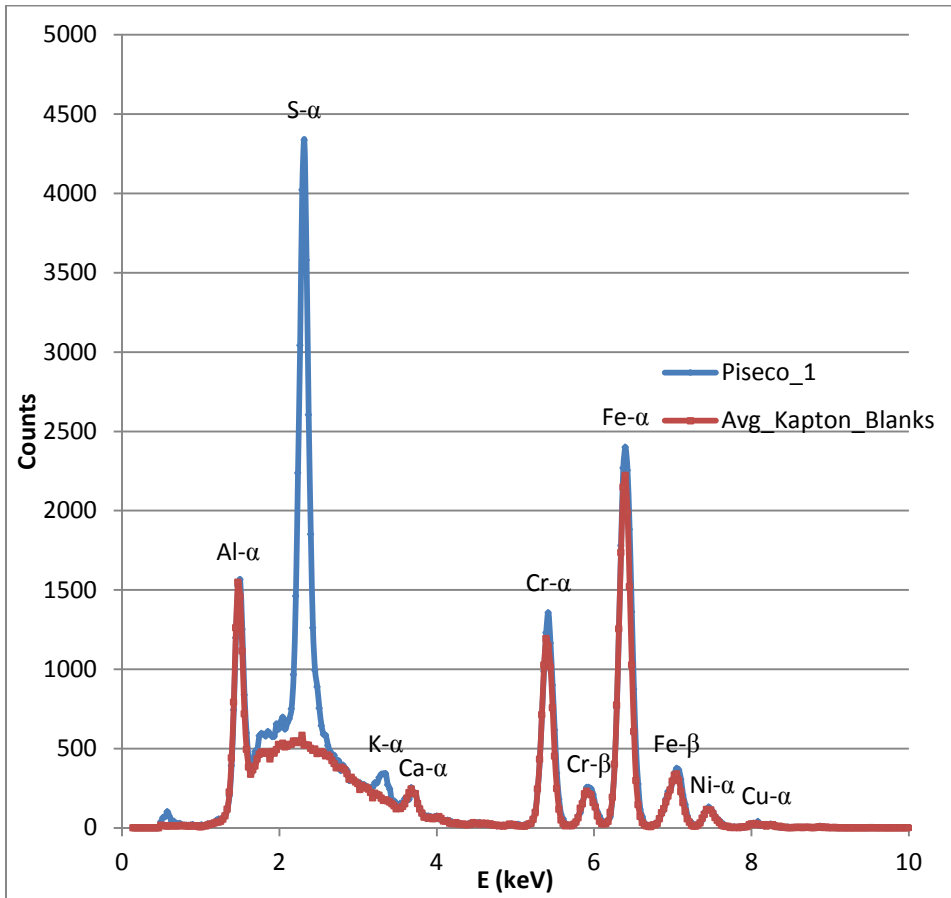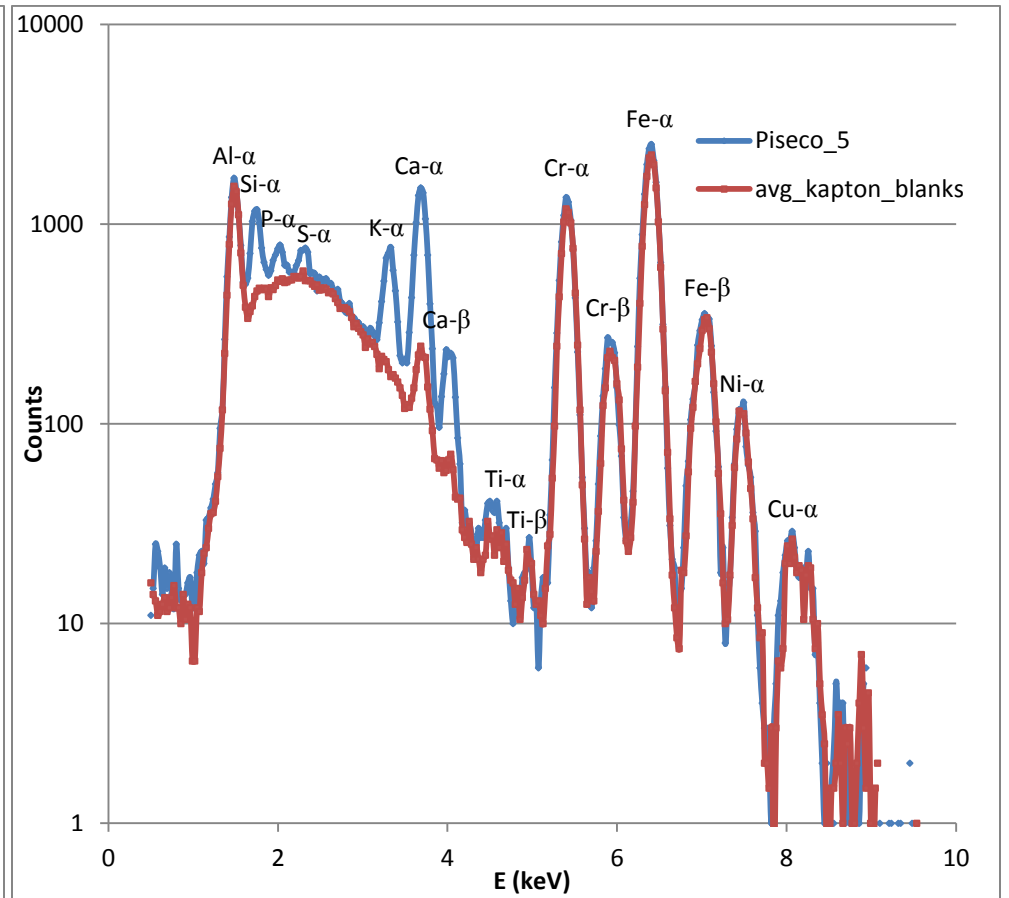
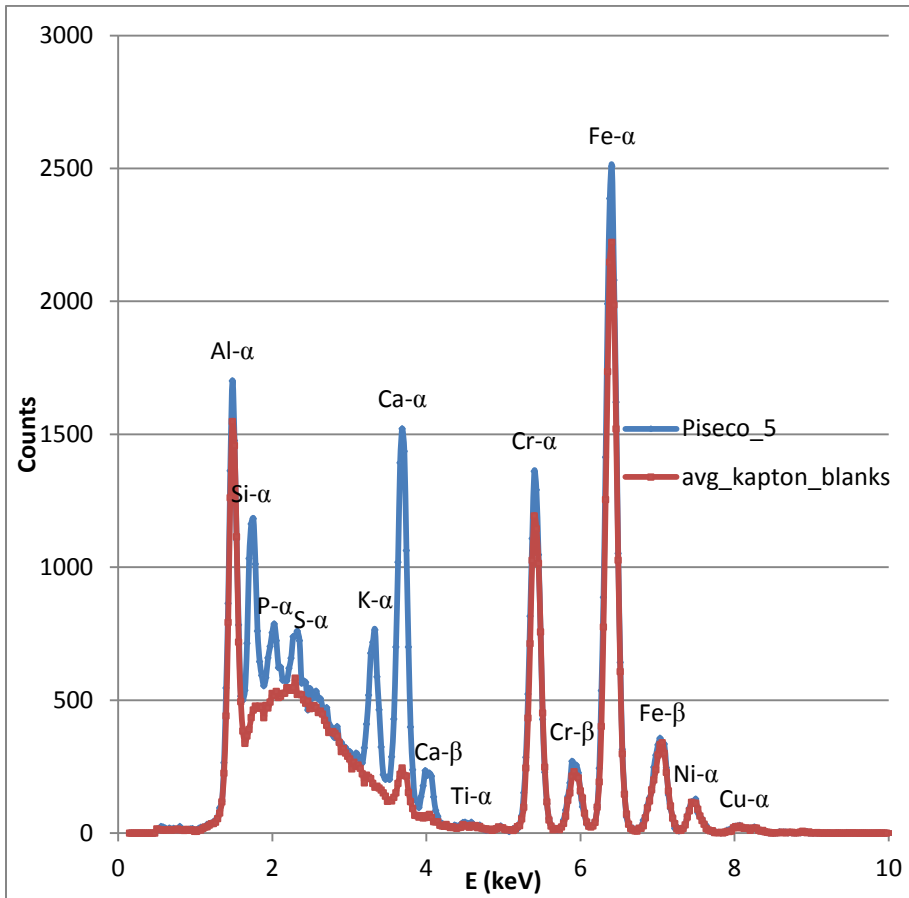July 2012, Impaction Stage 1 (PM 0.25 – 0.50 μm)
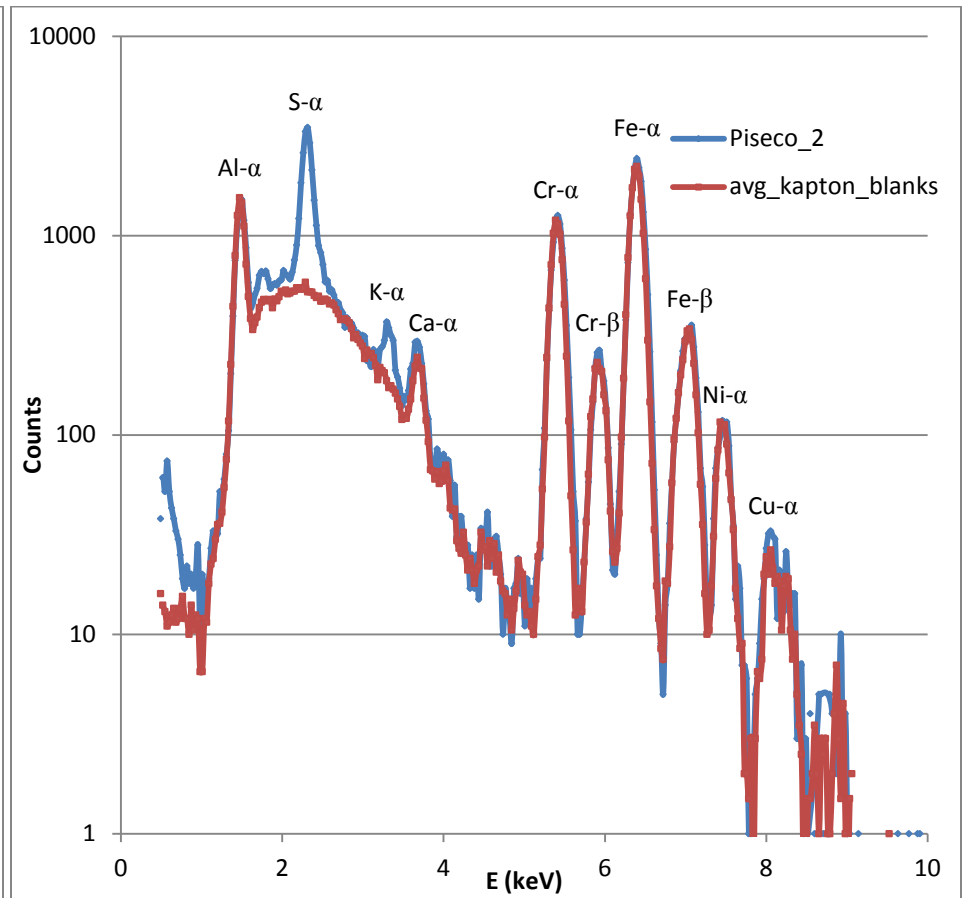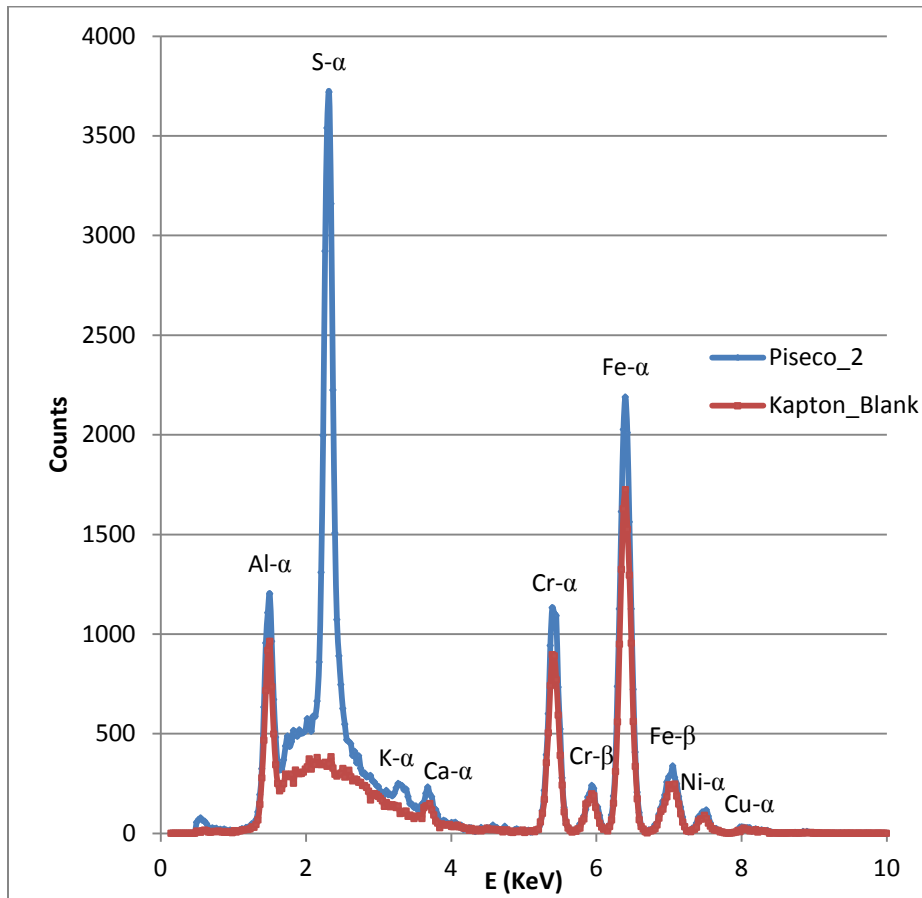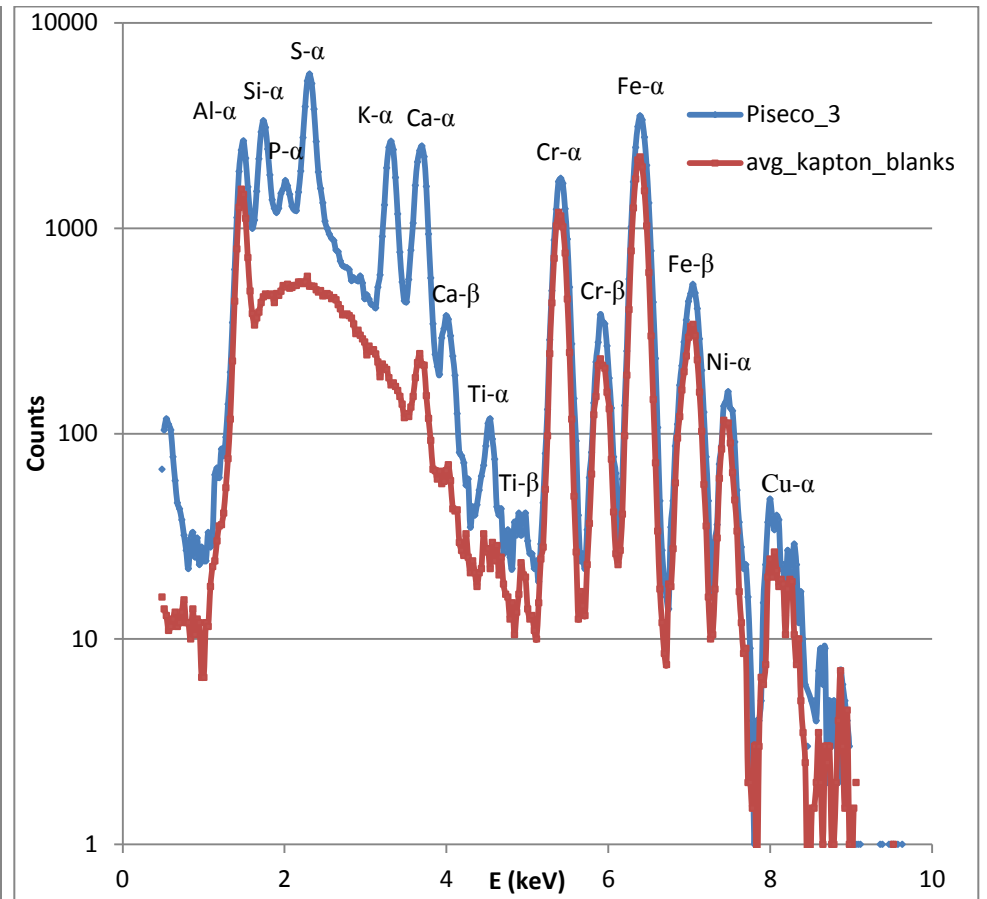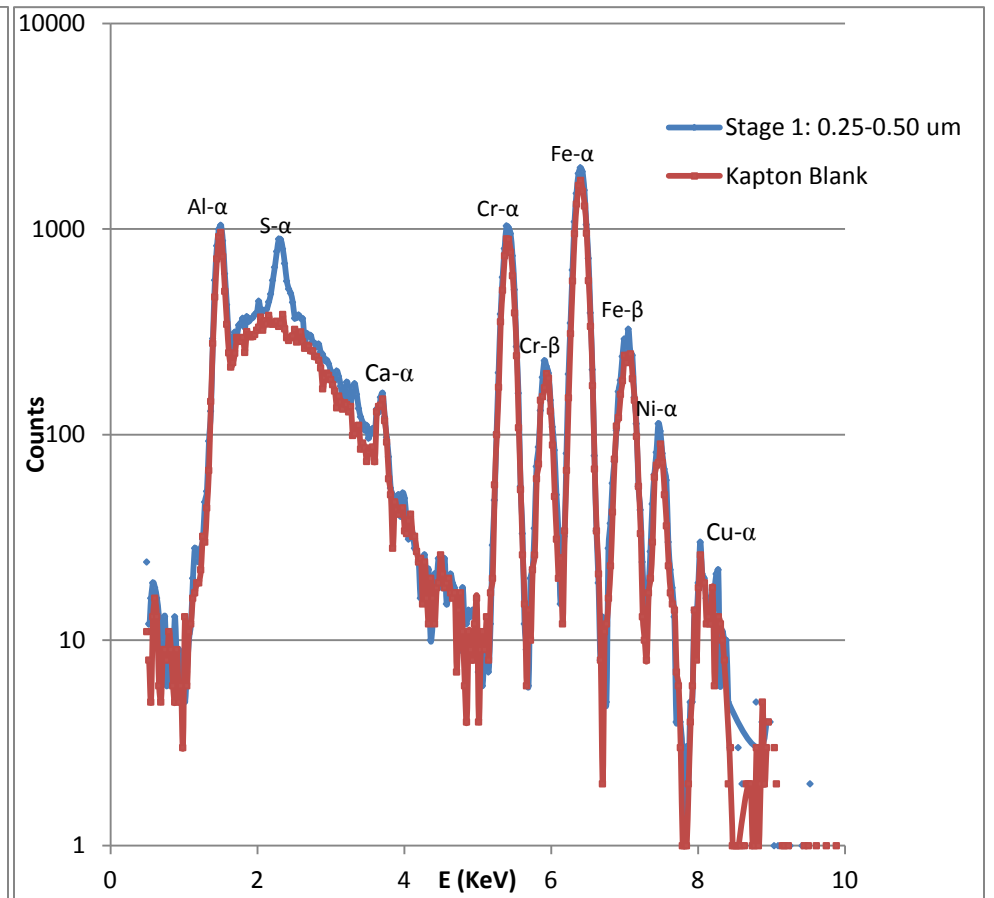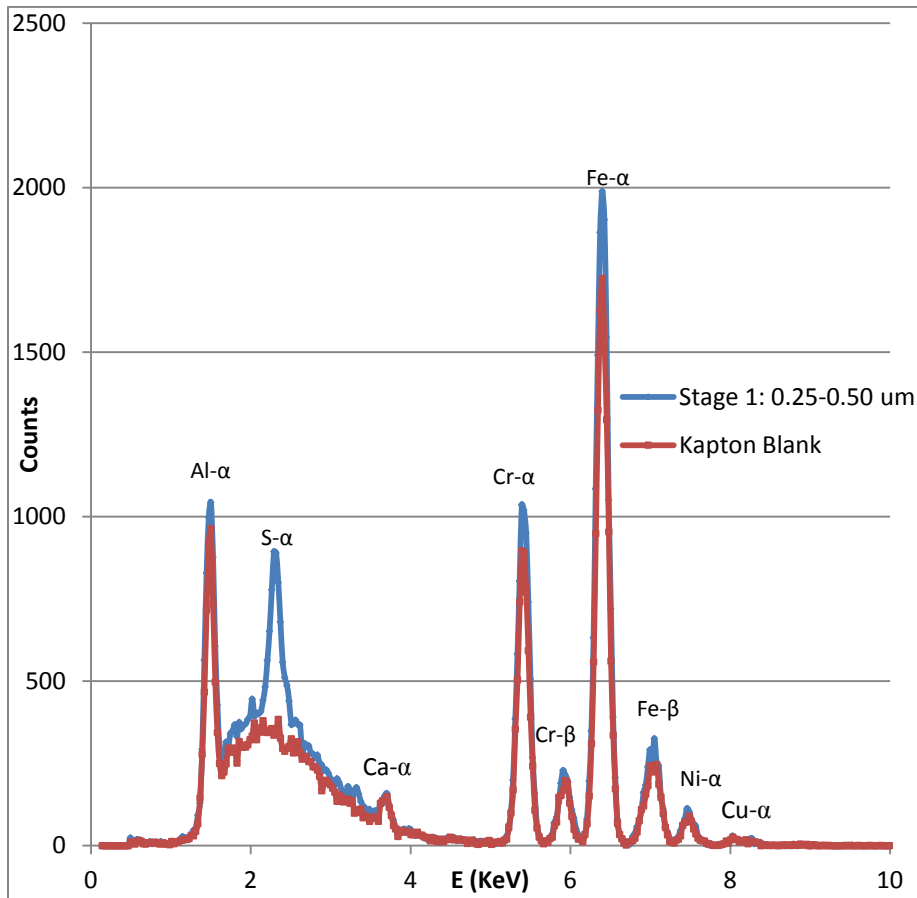
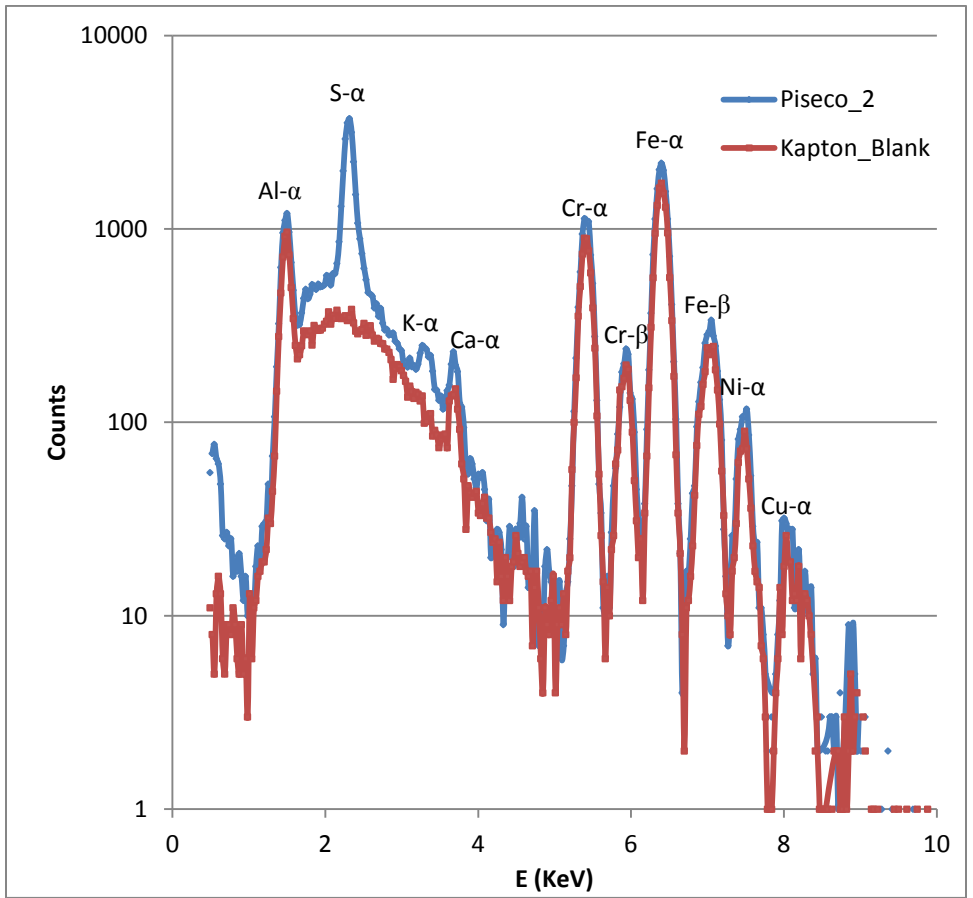July 2012, Impaction Stage 2 (PM 0.5 – 1.0 μm)

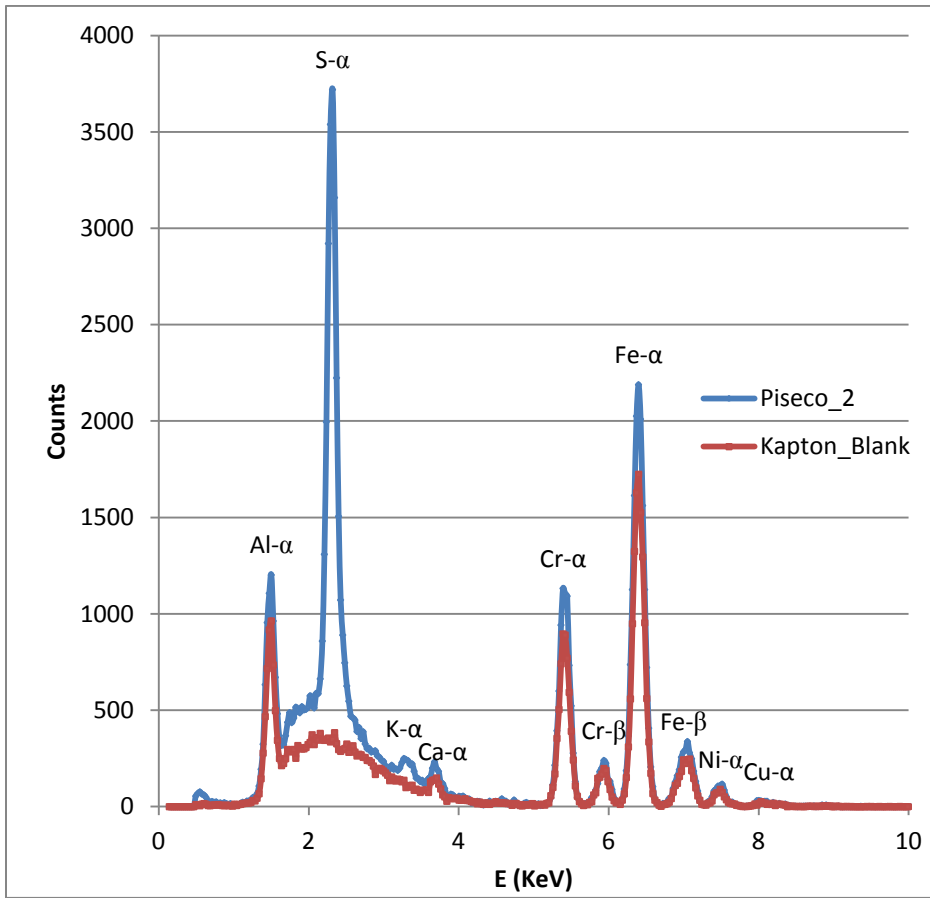July 2012, Impaction Stage 3 (PM 1 – 2 μm)
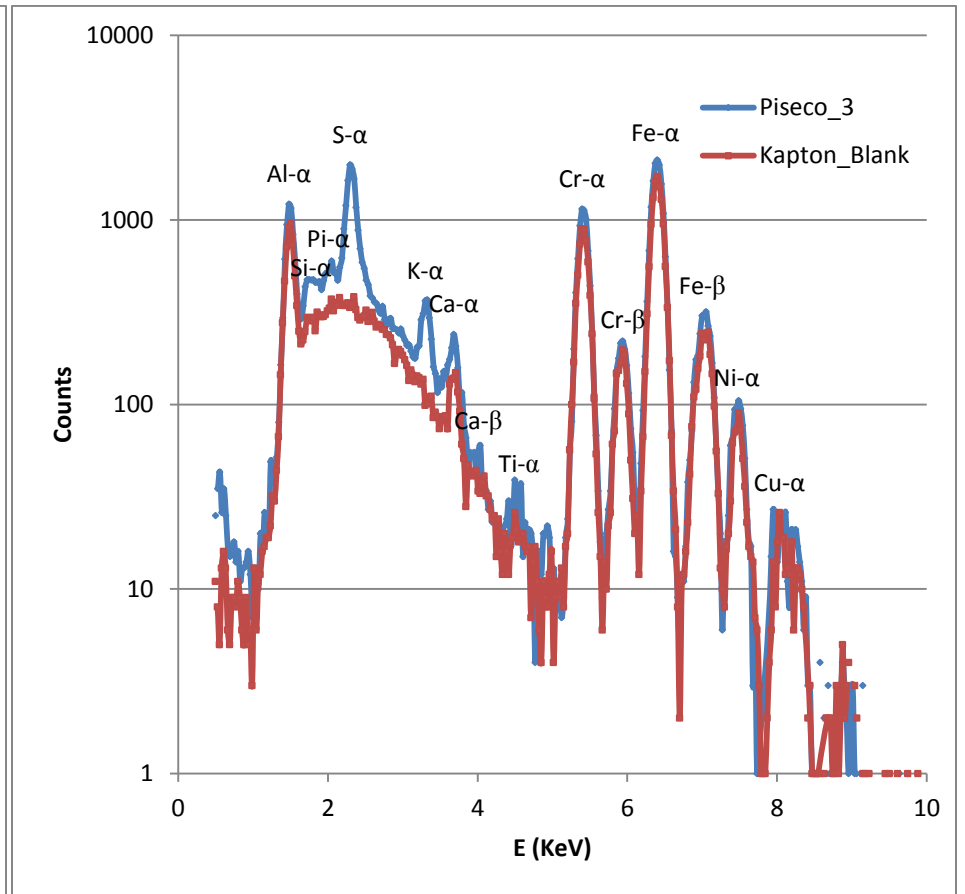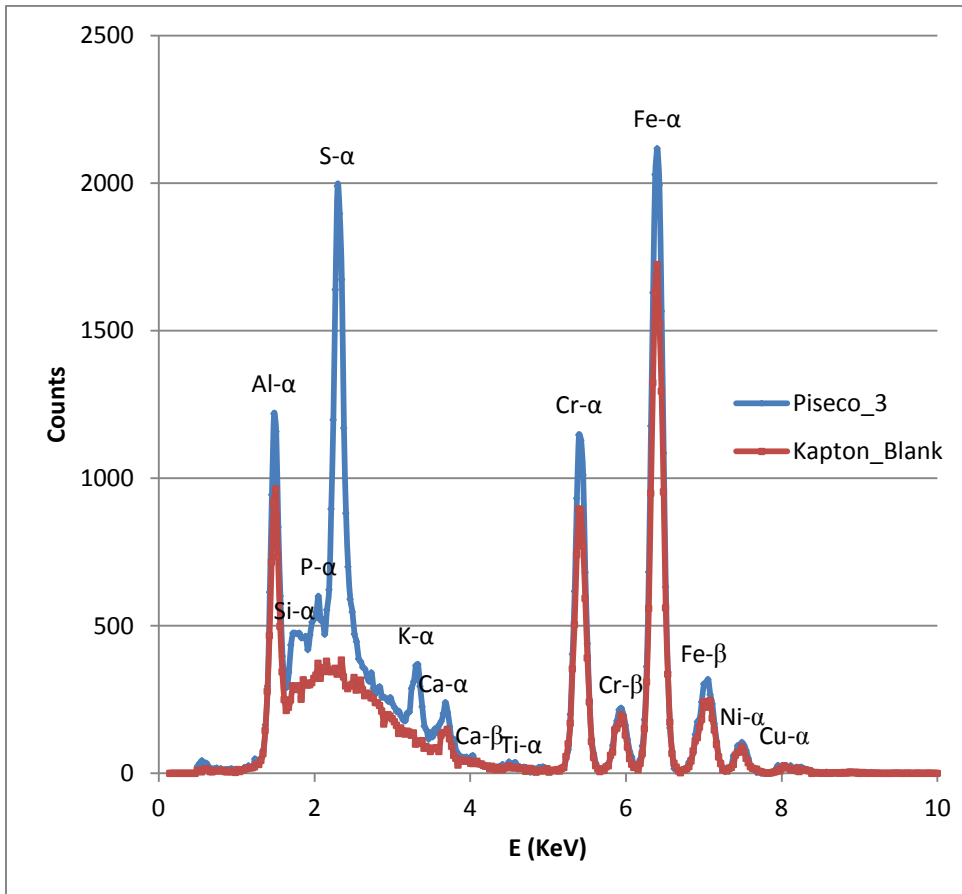
July 2012, Impaction Stage 4 (PM 2 – 4 μm)
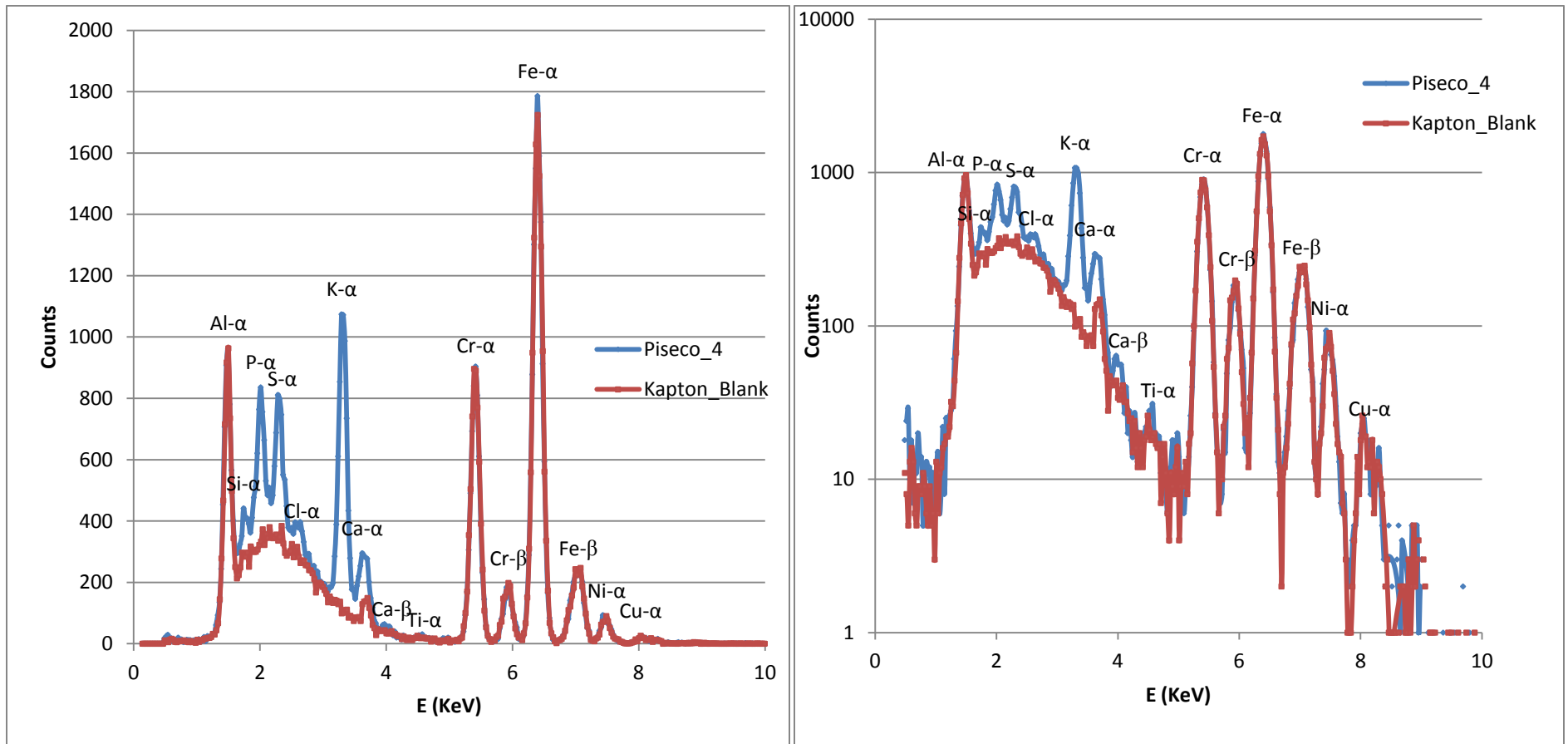
July 2012, Impaction Stage 5 (PM 4 – 8 μm)

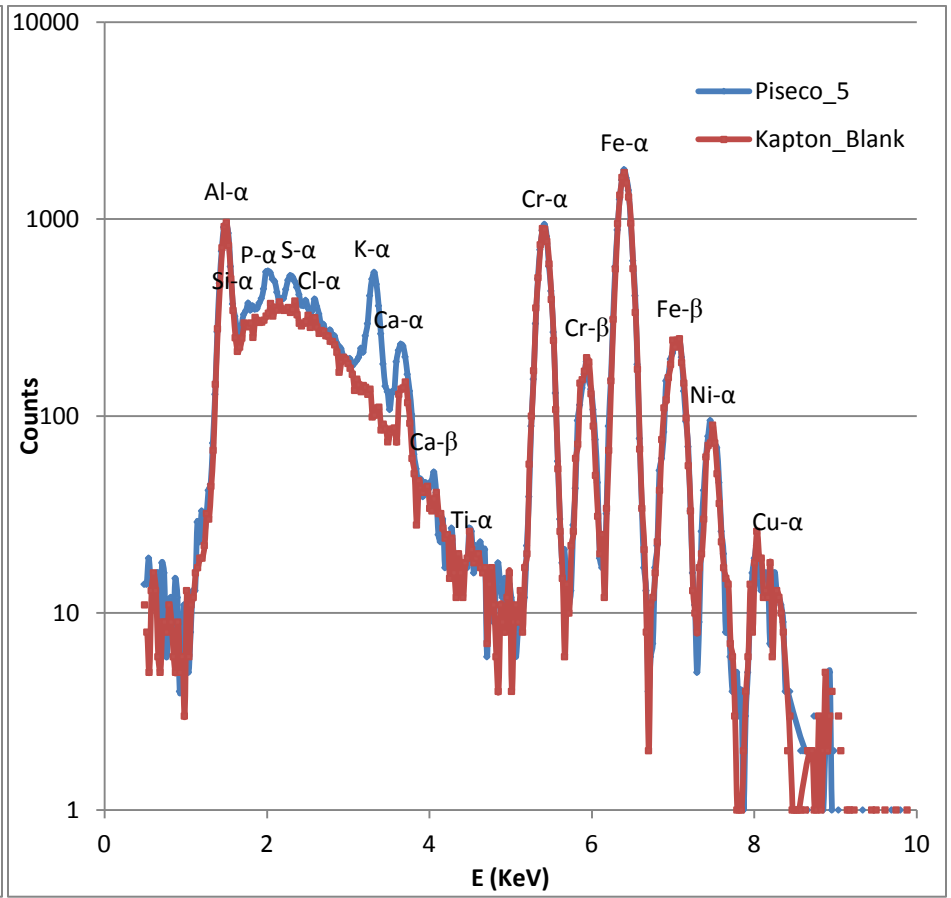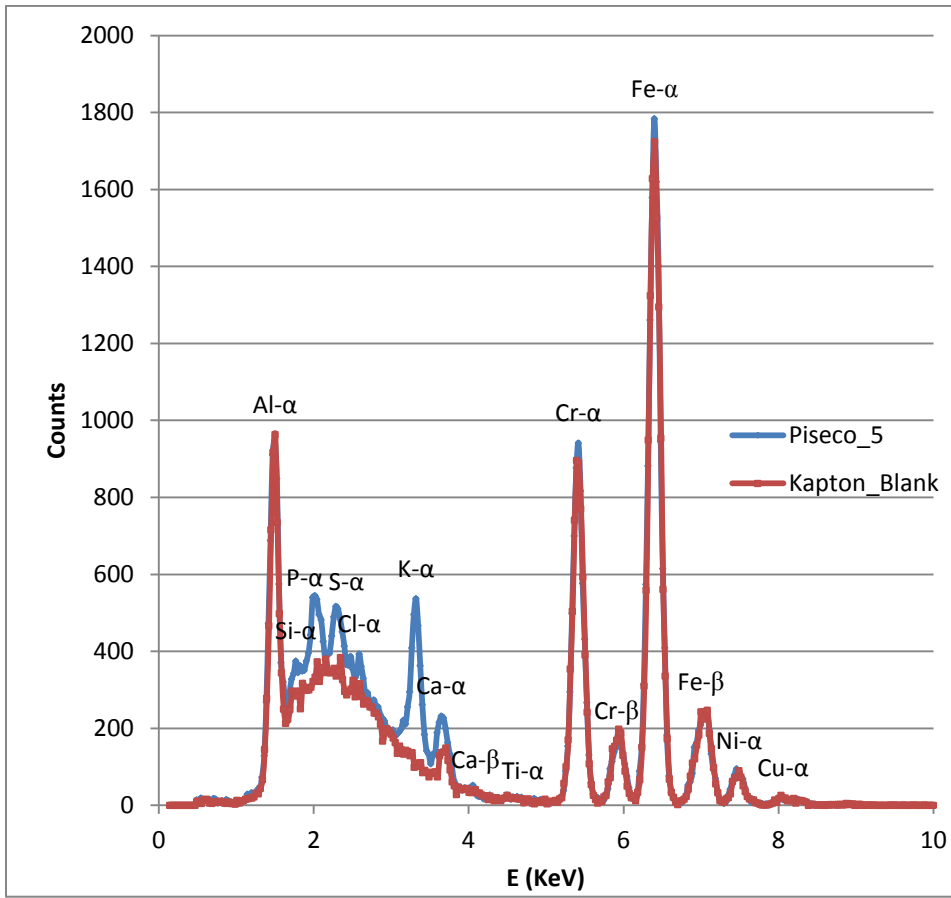September 2012, Impaction Stage 1 (PM 0.25 – 0.50 μm)

September 2012, Impaction Stage 2 (PM 0.5 – 1.0 μm)

September 2012, Impaction Stage 3 (PM 1 – 2 μm)

September 2012, Impaction Stage 4 (PM 2 – 4 μm)

September 2012, Impaction Stage 5 (PM 4 – 8 μm)

# Appendix 2

Uncertainty Propagation

GUPIX outputs two types of percentage errors with the concentrations: fit error, calculated on the basis of the final linear least-squares phase of the fit procedure with covariances; and statistical error, calculated on a square of counts basis. [11].  We used the fit error to propagate our uncertainty $\Delta C_A$ for all concentrations seen in Tables 4-5 and Figures 15-16.  This computation is shown below in Eq. 11-17.

As discussed on p. 16, the final areal mass density concentration was determined via the relation

$$C_A = C_{PI} - C_{BK},$$ Eq. 11

where $C_{PI}$ is the GUPIX concentration post-impaction and $C_{BK}$ is the concentration for the blank kapton foil.  Thus, we found the uncertainty in the areal mass density concentration as follows:

$$\Delta C_A = \sqrt{\left(\frac{\partial C_A}{\partial C_{PI}}\right)^2 (\Delta C_{PI})^2 + \left(\frac{\partial C_A}{\partial C_{BK}}\right)^2 (\Delta C_{BK})^2}$$ Eq. 12

$$= \sqrt{(\Delta C_{PI})^2 + (\Delta C_{BK})^2},$$ Eq. 13

where

$$\Delta C_{PI} = 0.01 * \Delta C_{PI_{GUPIX\,\%}} * C_{PI},$$ Eq. 14

and likewise, $\Delta C_{BK} = 0.01 * \Delta C_{BK_{GUPIX\,\%}} * C_{BK},$ Eq. 15

since GUPIX gave all errors in percentage form.  Furthermore, as we averaged over two blank kapton foils for July, we needed to add an extra propagation for $\Delta C_{BK_{July}}$ as follows.

$$\Delta C_{BK_{July}} = \sqrt{\left(\frac{\partial \Delta C_{BK_{July}}}{\partial \Delta C_{BK_{Kapton1}}}\right)^2 \left(\Delta C_{BK_{Kapton1}}\right)^2 + \left(\frac{\partial \Delta C_{BK_{July}}}{\partial \Delta C_{BK_{Kapton2}}}\right)^2 \left(\Delta C_{BK_{Kapton2}}\right)^2}$$ Eq. 16

$$= \sqrt{\left(\frac{1}{4}\right)\left(\Delta C_{BK_{Kapton1}}\right)^2 + \left(\frac{1}{4}\right)\left(\Delta C_{BK_{Kapton2}}\right)^2}.$$ Eq. 17

Finally, we used Eq. 10 to propagate the uncertainty $\Delta C_V$ in the mass per unit volume concentrations.  Since Eq. 10 only has repeated multiplication, we may simplify the standard expression with partials to get the following form:

45

$$\Delta C_{\mathrm{V}} = C_{\mathrm{V}} \sqrt{\left(\frac{\Delta T}{T}\right)^2 + \left(\frac{\Delta P}{P}\right)^2 + \left(\frac{\Delta A}{A}\right)^2 + \left(\frac{\Delta f}{f}\right)^2 + \left(\frac{\Delta t}{t}\right)^2 + \left(\frac{\Delta C_{\mathrm{A}}}{C_{\mathrm{A}}}\right)^2} \qquad \text{Eq. 18,}$$

where all variables are the same as in Eq. 10 and we assume no variance in the standard ambient temperature and pressure. The methodologies for obtaining all uncertainties in Eq. 18 are described above, p. 14-15 or in this appendix (for $\Delta C_{\mathrm{A}}$).